

BIOCHEMISTRY

Calmodulin disrupts plasma membrane localization of farnesylated KRAS4b by sequestering its lipid moiety

Benjamin M. M. Grant^{1,2}, Masahiro Enomoto¹, Sung-In Back^{1,2}, Ki-Young Lee¹, Teklab Gebregiorgis¹, Noboru Ishiyama¹, Mitsuhiro Ikura^{1,2*}, Christopher B. Marshall^{1*}

Copyright © 2020 The Authors, some rights reserved; exclusive licensee American Association for the Advancement of Science. No claim to original U.S. Government Works

KRAS4b is a small guanosine triphosphatase (GTPase) protein that regulates several signal transduction pathways that underlie cell proliferation, differentiation, and survival. KRAS4b function requires prenylation of its C terminus and recruitment to the plasma membrane, where KRAS4b activates effector proteins including the RAF family of kinases. The Ca²⁺-sensing protein calmodulin (CaM) has been suggested to regulate the localization of KRAS4b through direct, Ca²⁺-dependent interaction, but how CaM and KRAS4b functionally interact is controversial. Here, we determined a crystal structure, which was supported by solution nuclear magnetic resonance (NMR), that revealed the sequestration of the prenyl moiety of KRAS4b in the hydrophobic pocket of the C-terminal lobe of Ca²⁺-bound CaM. Our engineered fluorescence resonance energy transfer (FRET)-based biosensor probes (CaMeRAS) showed that, upon stimulation of Ca²⁺ influx by extracellular ligands, KRAS4b reversibly translocated in a Ca²⁺-CaM-dependent manner from the plasma membrane to the cytoplasm in live HeLa and HEK293 cells. These results reveal a mechanism underlying the inhibition of KRAS4b activity by Ca²⁺ signaling pathways.

INTRODUCTION

RAS-family small guanosine triphosphatases (GTPases) are key regulators of signal transduction pathways in cells, controlling proliferation, differentiation, survival, and apoptosis (1, 2). RAS proteins act as binary switches in response to external stimuli, cycling between an inactive, guanosine 5'-diphosphate (GDP)-bound, and active, guanosine 5'-triphosphate (GTP)-bound form, catalyzed by guanine nucleotide exchange factors and GTPase-activating proteins (3, 4). When localized to the inner leaflet of the plasma membrane (PM), RAS-GTP can bind to and activate several effector proteins involved in many cellular response pathways (1, 3–5). RAS genes (*HRAS*, *NRAS*, and *KRAS*) are mutated in roughly 30% of all human cancers (3, 4, 6), and *KRAS* is the most frequently mutated isoform, driving roughly 95% of pancreas, 45% of colon, and 31% of lung adenocarcinomas (7, 8). *KRAS* encodes two splice variants, *KRAS4a* and *KRAS4b*, of which the latter is more ubiquitously expressed and more extensively characterized.

RAS proteins share a highly conserved G-domain but are divergent at the C-terminal ~15 amino acids, designated the hypervariable region (HVR) (1, 3). The HVR of each isoform contains a unique combination of membrane localization signals, believed to be largely responsible for differential signaling and oncogenic capacity (4, 6, 8, 9). All isoforms contain a C-terminal CaaX box motif (C, cysteine; a, aliphatic; X, any residue), which is a target for irreversible farnesylation of cysteine, subsequent cleavage of the aaX residues, and carboxymethylation of the newly exposed C terminus (3, 10). *HRAS*, *NRAS*, and *KRAS4a* contain additional cysteines in the HVR that are reversibly palmitoylated, whereas *KRAS4b* membrane localization is enhanced through electrostatic interactions between the negatively charged membrane surface and a lysine-rich sequence in the HVR

called the polybasic region (Fig. 1A and fig. S1) (11–14). Because *KRAS4b* lacks palmitoylation sites, its affinity for the PM is lower than that of the other RAS isoforms (14).

RAS proteins are well-validated targets in oncology; however, they lack classic druggable pockets and have thus presented a major challenge to drug discovery efforts. A variety of indirect approaches to restrain RAS signaling have been pursued (15), largely unsuccessfully. Recognizing that prenylation of RAS is required for signaling, inhibitors of farnesyl transferases were developed; however, these ultimately failed in the clinic because of alternative prenylation of *KRAS4b* by geranylgeranyl transferases (16, 17). *KRAS4b* association with the PM is a particularly dynamic process that can be regulated by phosphodiesterase- δ (PDE δ) (18), a noncatalytic subunit of the photoreceptor PDE6. PDE δ binds the farnesylated HVR of cytoplasmic *KRAS4b* and delivers it to back to the PM through an active mechanism via recycling endosomes (19). Furthermore, a series of reports suggest that *KRAS4b* localization can be modulated by calmodulin (CaM) (20–24) and phosphorylation of Ser¹⁸¹ in the HVR (25–29). A need for novel approaches to inhibit *KRAS4b* signaling has generated interest in manipulating these systems to perturb the localization of *KRAS4b*. For example, inhibitors of the *KRAS4b* interaction with PDE δ have been shown to impair its oncogenic signaling (30, 31). Similarly, modulation of the CaM interaction with *KRAS4b* could potentially dampen its oncogenic properties, although a better understanding of this interaction is first required.

CaM is a ubiquitous calcium-sensing master regulator that binds a large and diverse group of targets, some in the presence and others in the absence of Ca²⁺, controlling many important biological pathways. CaM is a small (16.7 kDa), highly flexible protein characterized by two similar globular domains (lobes), each composed of two Ca²⁺-binding EF hands, separated by a flexible linker (32–34). Ca²⁺ binding to CaM induces a conformational change that exposes a methionine-rich hydrophobic pocket within each lobe (32–35). Canonical binding targets of Ca²⁺-CaM are helical, basic peptides with two hydrophobic “anchor” side chains separated by 2 to 18 residues, although CaM is remarkably plastic and has been shown to bind a

¹Princess Margaret Cancer Center, University Health Network, Toronto, Ontario M5G 1L7, Canada. ²Department of Medical Biophysics, University of Toronto, Toronto, Ontario M5G 1L7, Canada.

*Corresponding author. Email: mitsu.ikura@uhnresearch.ca (M.I.); chris.marshall@uhnresearch.ca (C.B.M.)

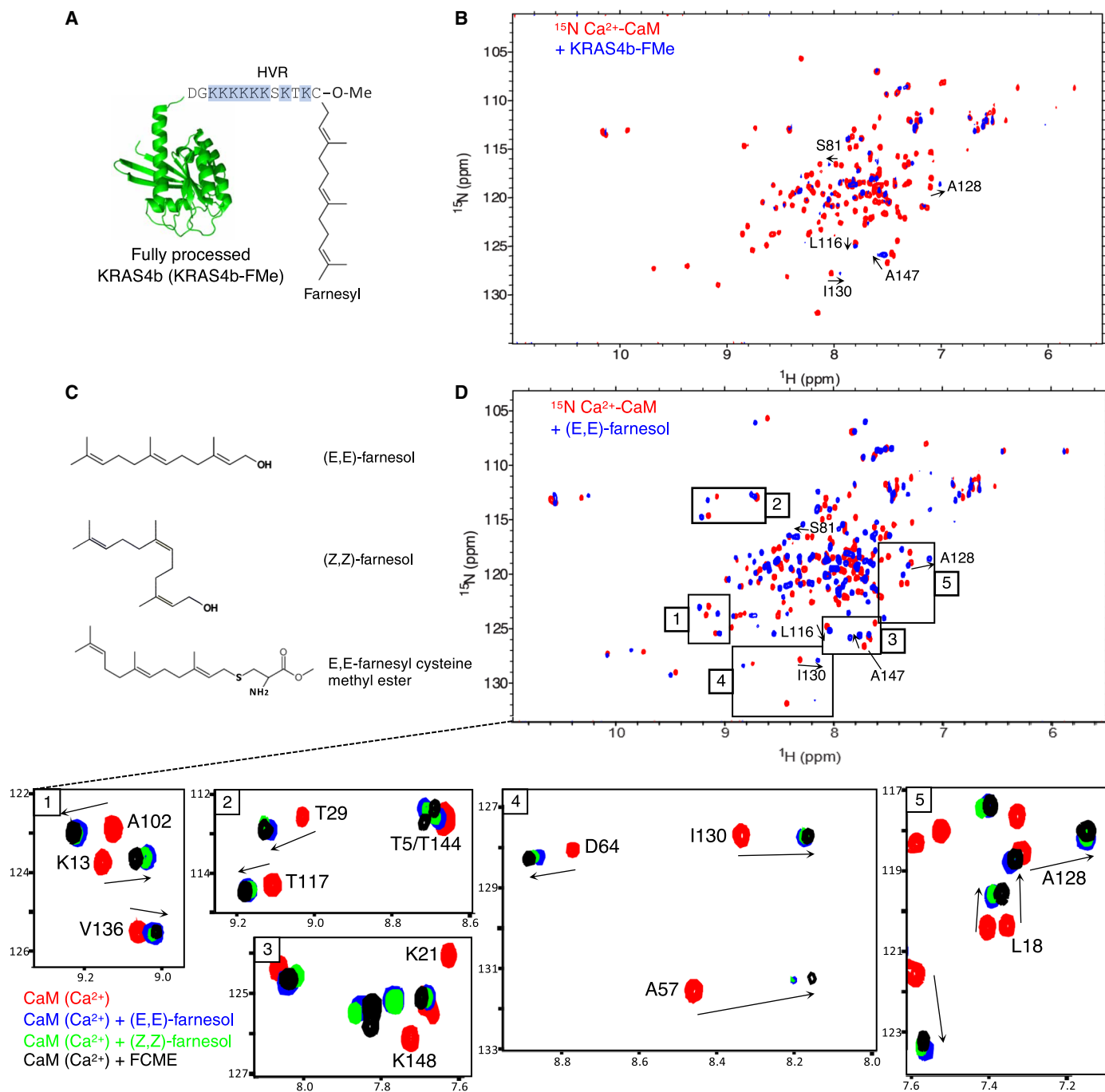


Fig. 1. CaM interacts strongly with farnesylated KRAS4b and farnesyl compounds. (A) Schematic of farnesylated KRAS4b purified from High Five insect cells engineered to enhance farnesylation capacity. The aaX (VIM) is cleaved off after farnesylation at Cys¹⁸⁵, and the exposed terminal cysteine is carboxymethylated. The polybasic region of the HVR is highlighted in blue. (B) ^1H - ^{15}N HSQC of uniformly ^{15}N -labeled CaM alone (red) and in the presence of fourfold excess KRAS4b-FMe-GDP (blue). The presence of KRAS4b-FMe induces CSPs and extensive signal broadening. Unbroadened signals that experience perturbations are highlighted (arrows) and used as probes for the interaction. (C) Chemical structures of tested farnesyl-derived compounds. (D) ^1H - ^{15}N HSQC of uniformly ^{15}N -labeled Ca $^{2+}$ -bound CaM alone (red) and in the presence of 11-fold excess (E,E)-farnesol (blue). Probe peaks from (B) are marked with arrows in the larger, full spectrum. Regions of the larger spectrum were extracted for a closer view in the boxes marked 1 to 5. All spectra were collected in NMR buffer containing 50 mM Hepes (pH 7.3), 100 mM NaCl, 10 mM Ca $^{2+}$, and 1 mM TCEP at 25°C and 600 MHz for eight scans. ppm, parts per million.

variety of noncanonical targets as well (32–34). The KRAS4b HVR is highly basic with propensity to form a helix but lacks hydrophobic anchor residues characteristic of a canonical CaM target.

Several groups have reported that CaM interacts with KRAS4b, but not with KRAS4a, HRAS, or NRAS, in a Ca $^{2+}$ -dependent manner, both in cells and in vitro, and that this modulates cell signaling

(20–24). In addition, it has been suggested that CaM binding extracts KRAS4b from the PM and is responsible for a relocalization to the cytoplasm and potentially internal membranes, altering signal output (21, 23, 25). However, there are contradictions in the literature regarding many of the details of this interaction. Various studies have reported that the interaction is GTP dependent (20, 36–38) and nucleotide independent (21, 23, 39, 40); farnesylation dependent (21, 23, 36, 38–40) and independent (20, 36, 37); and that the G-domain is either involved (20, 36, 38) or not (21, 23, 37, 39, 40). The effects of the interaction on KRAS4b localization and signaling have also been disputed (21, 23, 36, 39, 40). These inconsistencies have made it difficult for the field to reach a consensus about the nature and role of the interaction. Because of the plasticity of CaM and the lack of canonical CaM binding motifs in KRAS4b, very little is currently understood about the structural and biophysical properties of this complex.

In the first part of our study, we sought to investigate the structure and biophysical properties of the KRAS4b-CaM interaction *in vitro*. In particular, we examined Ca²⁺ and nucleotide dependence, identified interacting elements on both proteins, and assessed the ability of CaM to extract KRAS4b from lipid bilayers using a combination of nuclear magnetic resonance (NMR) and x-ray crystallography. Our NMR data show that CaM binding to KRAS4b is dependent on Ca²⁺ and KRAS4b farnesylation but found no evidence for involvement of the KRAS4b G-domain and no preference for the nucleotide bound to KRAS4b. A crystal structure of Ca²⁺-CaM in complex with a fragment of the processed HVR, farnesyl cysteine methyl ester (FCME), showed the farnesyl moiety buried deeply in the C-lobe hydrophobic pocket of CaM, providing a structural rationale for extraction of KRAS4b from the membrane by CaM. To validate this mechanistic model, we used live-cell microscopy using a chimeric CaM-KRAS4b fluorescence resonance energy transfer (FRET) probe designed on the basis of our structural data. This FRET-based biosensor enabled us to simultaneously monitor the interaction of CaM with KRAS4b and intracellular translocation of the complex upon stimulation of a cellular Ca²⁺ signal in both HeLa and human embryonic kidney–293 (HEK293) cells. We demonstrate that increased intracellular calcium stimulates KRAS4b translocation from the PM to the cytoplasm, which is spatially and temporally regulated via Ca²⁺-CaM in mammalian cells.

RESULTS

KRAS4b-CaM interaction is dependent on farnesylation

Some reports have described an interaction between CaM and unfarnesylated KRAS4b (20, 36, 37); thus, we began to test the interaction using unprocessed KRAS4b expressed in *Escherichia coli* (residues 1 to 185, representing the full-length protein after -aaX cleavage but lacking farnesylation and carboxymethylation). We collected ¹H-¹⁵N heteronuclear single quantum correlation (HSQC) NMR spectra of ¹⁵N-labeled KRAS4b or ¹⁵N-CaM and analyzed chemical shift perturbations (CSPs) upon the addition of the other unlabeled protein. These experiments were performed with KRAS4b in both GDP- and GTPγS-loaded states and in the presence and absence of Ca²⁺. In the presence of Ca²⁺, a few minor CSPs were observed in both proteins independent of which nucleotide was bound; however, no large CSPs that would be indicative of a strong or specific interaction were detected (fig. S2, A to D). Some of these small CSPs were likely because of nonspecific electrostatic interactions between the basic lysine residues in the HVR and the acidic surface of CaM. Notably, the CSPs in

both proteins were more appreciable when KRAS4b was GTP-loaded. Binding to GTP primes RAS for interaction with its binding partners, which may likewise make it more prone to nonspecific interactions as well. Nevertheless, we do not consider these minor changes relevant in comparison to the large CSPs typically observed upon binding of CaM to canonical targets such as protein kinases and or channels (41–43). Hence, we conclude that CaM only makes weak transient contacts with unfarnesylated KRAS4b in solution.

To determine whether CaM binds to farnesylated KRAS4b, we examined the interaction of CaM with full-length, fully processed KRAS4b (designated KRAS4b-FMe, which is farnesylated and has the C-terminal tripeptide removed and the Cys¹⁸⁵ carboxymethylated, as illustrated in Fig. 1A) expressed in and purified from insect cells using a baculovirus expression protocol developed by National Cancer Institute (NCI) Frederick (44). In contrast to the unfarnesylated protein, addition of KRAS4b-FMe to ¹⁵N-CaM in the presence of Ca²⁺ induced widespread changes in the ¹⁵N-CaM spectrum, affecting most of the cross-peaks (Fig. 1B). Specifically, KRAS4b-FMe induced severe line broadening of ~80% of the CaM resonances and CSPs in several of the peaks that were not broadened beyond detection, indicating a farnesyl-dependent interaction between KRAS4b-FMe and CaM. The peak broadening is likely caused by several factors, including the increased molecular mass of the complex, transient exchange between bound and unbound states, and chemical exchange from nonspecific contacts between the G-domain of KRAS4b and CaM. The broadening of NMR signals upon titration of KRAS4b-FMe into CaM has been corroborated (40). Several residues within the C-lobe, Ser⁸¹, Leu¹¹⁶, Ala¹²⁸, Ile¹³⁰, and Ala¹⁴⁷, exhibited chemical shift changes, indicative of a more stable and specific interaction (Fig. 1B, arrows). Although the CSPs provide probes of the interaction, the extensive signal broadening limited the structural information that could be extracted from these spectra. Therefore, to improve spectral quality and gain insights into the structural mechanism, we sought to identify the minimal binding elements that mediate the interaction between KRAS4b-FMe and CaM.

Farnesyl moiety is sufficient for CaM binding

With the knowledge that farnesylation is necessary for the KRAS4b-CaM interaction, we first questioned whether the farnesyl moiety alone is sufficient for CaM binding. Using a series of farnesyl-derived compounds (Fig. 1C), we assessed CSPs in the ¹H-¹⁵N HSQC spectra of CaM. First, (E,E)-farnesol, an alcohol derivative of the primary stereoisomer present in mammalian cells, was solubilized in dimethyl sulfoxide (DMSO) and titrated into ¹⁵N-CaM in the presence of Ca²⁺. The resulting ¹H-¹⁵N HSQC spectra exhibited extensive CSPs of almost all cross-peaks, indicating that CaM undergoes a substantial structural rearrangement upon addition of (E,E)-farnesol (Fig. 1D). During titration of farnesol, CaM peaks did not exhibit the broadening caused by KRAS4b-FMe titration, and the five probe peaks identified above exhibited similar chemical shift changes in both spectra. A previous titration of Ca²⁺-CaM with a farnesylated KRAS4b C-terminal 6-mer peptide (KSKTKC-FMe) produces a CaM spectrum nearly identical to ours in the presence of farnesol alone (40), suggesting that the farnesyl moiety may recapitulate the KRAS4b-CaM binding mode. The spectrum also resembles those of Ca²⁺-CaM in complex with myristoylated polybasic peptides (fig. S3) (45, 46). Farnesol titration does not cause peak broadening due to its smaller size and the absence of chemical exchange between CaM and a dynamic G-domain. The chemical shift changes have been plotted by

residue and mapped onto the surface of CaM (fig. S4). In the absence of Ca^{2+} , no CSPs were apparent, indicating that this interaction is fully Ca^{2+} dependent (fig. S5), consistent with every previous report of the KRAS4b–CaM interaction.

To investigate the stereospecificity of this lipid:CaM interaction, we titrated the natural, rare stereoisomer (Z,Z)-farnesol (Fig. 1C) into ^{15}N -CaM. The CaM spectra in the presence of the two stereoisomers were very similar (Fig. 1E), suggesting that structural plasticity of CaM can accommodate either conformation of the lipid by virtue of the flexible linker and malleable methionine-rich hydrophobic pockets (33, 47, 48). We titrated ^{15}N -CaM with (E,E)-FCME (Fig. 1C), comprising the fully processed C-terminal residue of KRAS4b, which showed that extension of farnesol to include the carboxymethylated cysteine moiety caused minor changes in the pattern of CSPs (Fig. 1E) and promoted saturation at a lower molar ratio, suggesting that this amino acyl component contributes to binding affinity. Last, all assigned CaM peaks could be traced to saturation throughout the titrations with farnesyl compounds (fig. S6) and were found to overlay with the subset of CaM peaks that remained visible upon titration with KRAS4b-FMe (fig. S7), suggesting that CaM interaction with the lipid comprises the core of the KRAS4b-FME–CaM complex (schematic in Fig. 2A). This finding is supported by a previous crystal structure of Ca^{2+} -CaM in complex with the myristoylated N-terminal polybasic peptide from CAP23/NAP22, in which the myristoyl moiety is directly sequestered (49), but the relative contribution of the peptide versus lipid moieties to CaM binding was not assessed.

Crystal structure of CaM in complex with FCME reveals C-lobe binding

To obtain an atomic-resolution picture of the interaction, we used x-ray crystallography. Multiple crystallization trials (~300 conditions) of Ca^{2+} -CaM complexed with (E,E)-farnesol were unsuccessful; however, the FCME complex produced crystals in 66 conditions, suggesting that the cysteine moiety in FCME may be involved in the specificity of binding, thus reducing structural heterogeneity. One of these conditions was optimized (see Materials and Methods), and the best crystal was diffracted to 1.8 Å and 2.0 Å with anomalous data, using a synchrotron x-ray source. Initially, density maps were generated separately by (i) molecular replacement using a structure of CaM bound to the myristoylated CAP23/NAP22 peptide [Protein Data Bank (PDB): 1L7Z] (49) as a search model and (ii) a priori with experimental phasing from anomalous data, primarily scattered by Ca^{2+} ions. Both approaches yielded highly similar structures. The two datasets were combined in HKL2000 and refined in Phenix to yield a high-resolution map of the CaM-FCME complex (crystallographic statistics found in Table 1).

In this structure, the N- and C-lobes of CaM come together to form a compact globular conformation with a hydrophobic core and acidic surface (Fig. 2, B and C), akin to many reported structures of CaM-target complexes (50). Our structure is globally similar to that of CaM in complex with the myristoylated CAP23/NAP22 peptide; however, several differences are apparent (fig. S8A). In the CAP23/NAP22 structure, the saturated, unbranched myristoyl moiety extends through a hydrophobic channel formed by both lobes, whereas our structure shows the farnesyl moiety of FCME, which is unsaturated and branched, buried deep within the C-lobe hydrophobic pocket of CaM (Fig. 2, D and F), and the N-lobe pocket is minimally exposed (fig. S8B). It is clear from the electron density that the farnesyl moiety is exclusively anchored within the C-lobe pocket, although multiple

conformations likely coexist. In the major conformation, the cysteine moiety of FCME protrudes through an opening between α -helices 1, 6, and 7 (Fig. 2B and fig. S9A), whereas weak additional electron density suggests that FCME may exist in an alternate low-occupancy conformation in which the aminoacyl end exits the hydrophobic core from the opposite side. The major conformer exhibits strong, well-defined electron density (fig. S9, B and C), and the C-terminal cysteine residue occupies a position equivalent to that of the N-terminal myristoylated glycine in CAP23/NAP22; thus, the adjacent polybasic sequences would be tethered in the same region in both complexes, albeit with opposite strand directions.

This structure indicates that CaM sequesters the farnesyl moiety in its hydrophobic core and suggests that electrostatic interactions may form between the acidic surface of CaM (accessible acidic residues include Asp⁷, Asp¹¹, Asp¹⁴, Asp¹¹⁴, Asp¹²⁰, Asp¹²³, and Asp¹²⁷ and the linker, Asp⁸², Asp⁸³, and Asp⁸⁴) and the basic HVR of KRAS4b (Fig. 2C), whereas this interaction does not directly involve the G-domain. To gain more insight into this structure in solution, we performed NMR experiments using a paramagnetic relaxation enhancement (PRE) probe in which a 2,2,6,6-tetramethylpiperidine 1-oxyl (TEMPO) spin-labeled molecule was conjugated to the free-amine group of FCME (51, 52). TEMPO-FCME was added to ^{15}N -CaM in solution, and ^1H - ^{15}N HSQC spectra were recorded (fig. S10A). Many resonances were broadened by the spin label, but the subset of peaks that were not broadened overlaps the spectrum of CaM bound to untagged FCME, indicating that the TEMPO tag has minimal impact on the interaction of CaM with TEMPO-FCME. The residues associated with PRE-induced peak broadening were mapped onto our crystal structure (fig. S10, B and C). The largest PRE effect was observed for those residues near the α 1,6,7 exit site, and another less intense PRE cluster was observed around the putative alternate exit site. This PRE broadening around α 1,6,7 involves both lobes, consistent with our crystal structure and supporting the presence of a compact CaM configuration with interlobe contacts in solution.

Membrane and CaM binding of KRAS4b are mutually exclusive

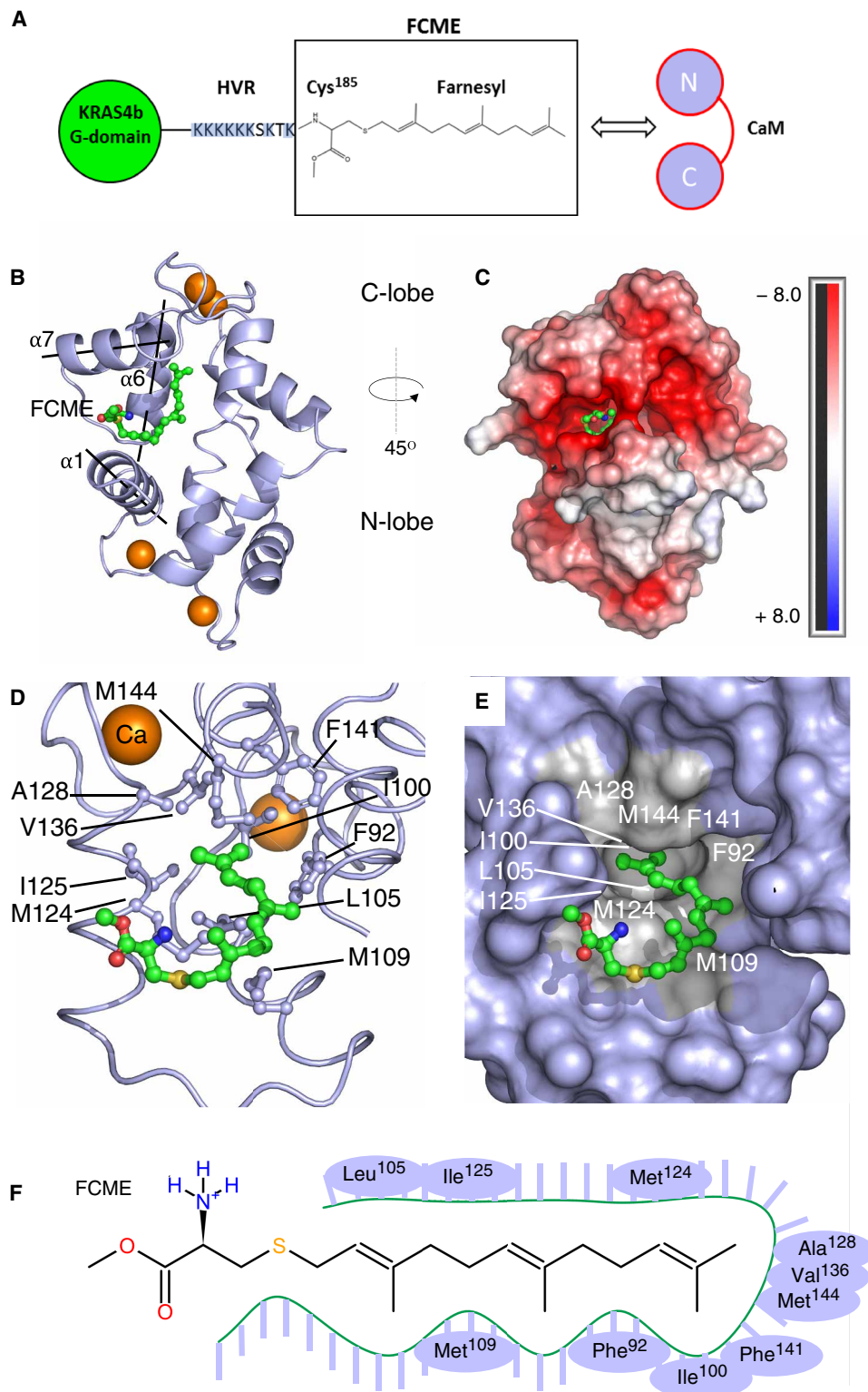
Because the farnesyl group and the HVR both contribute to KRAS4b membrane localization, we sought to determine whether KRAS4b binding with CaM and with lipid bilayers is compatible or mutually exclusive. We used ^{15}N -lysine-labeled KRAS4b-FMe to probe the HVR, as it contains nine lysine residues in the terminal 15 amino acids. As previously described, we performed NMR experiments to investigate the KRAS4b interaction with membranes using a synthetic lipid bilayer nanodisc (ND) composed of 80% dioleoylphosphatidylcholine (DOPC) and 20% dioleoylphosphatidylserine (DOPS) (53). Five signals from lysine backbone amides in the KRAS4b-FMe HVR are well resolved and assignable from previous work (Fig. 3A) (54). Upon binding to ND (1:5 ND: KRAS4b-FMe), these signals disappear, presumably due to broadening from rapid chemical exchange as a result of transient electrostatic interactions between KRAS4b-FMe (farnesyl and the HVR) and the negative surface of the ND (Fig. 3B). Subsequent addition of Ca^{2+} -CaM to this sample restored the intensity of these HVR lysine signals (Fig. 3C), and the resulting spectrum overlays with that of ^{15}N -lysine KRAS4b-FME complexed with Ca^{2+} -CaM in the absence of NDs (Fig. 3D), which is distinct from the spectrum of KRAS4b-FME alone in solution (Fig. 3E). These data demonstrate direct competition between NDs and CaM for KRAS4b-FME binding, consistent with the fact that they share the same interacting elements. This is also consistent with the reported affinity of CaM for KRAS4b-FME [dissociation

Fig. 2. Crystal structure of CaM in complex with FCME. (A) Schematic diagram of the CaM-KRAS4b-FMe interaction based on the NMR data presented in Fig. 1; the hydrophobic core of CaM sequesters the farnesyl moiety of KRAS4b-FMe.

(B to E) X-ray crystallography structure of Ca^{2+} -CaM bound to FCME, resolved to 1.8 Å (PDB: 6OS4). The cartoon diagram of the CaM-FCME structure (B) shows a compact CaM conformation with significant interlobe contacts. FCME is buried in the CaM C-lobe hydrophobic pocket with the aminoacyl (C^{185}) group exiting through a gap between α -helices 1, 6, and 7. The surface electrostatic representation of CaM (C) shows the channel formed by α -helices 1, 6, and 7 through which the cysteinyl moiety of FCME exits [rotated 45° relative to (B)] and the highly acidic surface accessible to an adjacent polybasic HVR. Electrostatics were modeled with the APBS PyMol plugin. Panel (D) shows a zoomed perspective of FCME in the CaM C-lobe hydrophobic pocket [rotated 90° relative to (B), into the interlobe plane]. Ten residues involved in hydrophobic contacts with the ligand are depicted as sticks and labeled. Panel (E) shows a close-up surface representation of FCME in the C-lobe hydrophobic pocket [oriented as in (D)] with interacting residues colored gray. (F) A ligand interaction map highlighting the hydrophobic interactions between FCME and the CaM C-lobe pocket.

constant (K_d) of 0.3 to 0.4 μM] (40), which is an order of magnitude higher than the KRAS4b-FMe affinity for the lipid bilayer (K_d of 4 μM) (44).

To further validate this observation, we used PRE experiments to directly track KRAS4b-FMe membrane association. As previously described (54, 55), we monitored the signals of ^{13}C -methyl-labeled KRAS4b-FMe (a total of 92 methyls from Thr/Ile/Leu/Val/Met are labeled) in the presence and absence of NDs containing an embedded Gd^{3+} -chelating lipid. This scheme enabled us to identify, through PRE-induced line broadening, the extent of the interaction of KRAS4b-FMe with the membrane surface (schematic in Fig. 3F). In the presence of NDs and Ca^{2+} -free CaM, peaks from several residues—especially Ile²⁴, Val²⁵, Ile⁵⁵, and Leu¹¹³—which are proximal to the membrane surface in the GDP-bound state (54, 55), were strongly broadened. Addition of Ca^{2+} alleviated the PRE effect on KRAS4b-FMe, restoring peak intensities, consistent with a loss of membrane association of KRAS4b-FMe in the presence of Ca^{2+} -CaM (Fig. 3G; full plots in fig. S11, A and B). Together, these results indicate that Ca^{2+} -CaM effectively extracts KRAS4b-FMe from membranes via the sequestration of the farnesyl group in a Ca^{2+} -dependent manner.



CaM-KRAS4b chimera construct displays Ca^{2+} -dependent FRET in vitro

To observe the interaction between KRAS4b-FMe and CaM and monitor the localization of the proteins in cells, we prepared constructs encoding these proteins as fusions with FRET donor/acceptor

Table 1. Crystallographic statistics reported for deposited CaM-FCME complex structure (PDB: 6O54). This crystal was grown at room temperature in 0.2 mM sodium acetate, 0.1 mM sodium cacodylate (pH 6.7), and 28% PEG 8000, with 1.25 mM CaM and 5 mM FCME, using the sitting drop-vapor diffusion method. The protein crystal was diffracted on the Canadian Macromolecular Crystallography Facility 08ID-1 Beamline at the Canadian Light Source at two wavelengths to collect native ($n = 1$) and anomalous scattering ($n = 1$) datasets, which were processed using HKL2000 and refined with Phenix. Values in parentheses are for the highest resolution shell. a, b, c, unit cell measurements; α , β , γ , unit cell angles; RMS, root mean square.

6O54	Native FP2, SigFP2	Anomalous I(+), SigI(+), I(-), SigI(-)
Wavelength	1 Å	1.77 Å
Resolution range	34.78–1.81 (2.01–1.81)	34.78–2.05 (2.123–2.05)
Space group	P 61 2 2	P 61 2 2
Unit cell: a, b, c α , β , γ	40.379, 40.379, 338.137 90, 90, 120	40.379, 40.379, 338.137 90, 90, 120
Total reflections	16289*	19319*
Unique reflections	11386 (1091)	11372 (1075)
Multiplicity		
Completeness (%)	99.91 (99.63)	99.84 (98.71)
Mean I/sigma(I)	28*	19.2*
Wilson B factor	35.15	42.8
Reflections used in refinement	11380 (1087)	11370 (1075)
Reflections used for R-free	1139 (109)	1138 (108)
R-work	0.2024 (0.1934)	0.1912 (0.2200)
R-free	0.2418 (0.2195)	0.2253 (0.2586)
Number of nonhydrogen atoms	1194	1194
Macromolecules	1107	1107
Ligands	27	27
Solvent	60	60
Protein residues	144	144
RMS (bonds)	0.006	0.006
RMS (angles)	0.75	0.75
Ramachandran favored (%)	98.59	98.59
Ramachandran allowed (%)	1.41	1.41
Ramachandran outliers (%)	0	0
Rotamer outliers (%)	1.83	1.83
Clash score	0.93	0.93
Average B factor	47.67	47.67
Macromolecules	47.12	47.12
Ligands	78.13	78.13
Solvent	44.21	44.21

*Results from Phenix Xtriage.

fluorophores—mTurquoise2 (mTq2) and super yellow fluorescent protein 2 (SYFP2) (i.e., mTq2-CaM and SYFP2-KRAS4b)—and transiently coexpressed them in HeLa and HEK293 cells. To increase the expression of KRAS4b to levels achieved for CaM, it was necessary to optimize the codon usage by removing rare codons (56, 57). Overexpression of CaM is toxic to cells due to its perturbation of death-associated pathways (58); thus, coexpression of KRAS4b and CaM resulted in morphological changes in HeLa cells, including cell rounding, detachment, and cell death 1 to 2 days after transfection. These effects were mitigated by fusing the

proteins into a chimeric construct (mTq2-CaM-SYFP2-KRAS4b). Because both KRAS4b and CaM have multiple interaction partners, linking the two proteins may favor the intramolecular interaction over other binding partners while also ensuring equimolar expression of KRAS4b and CaM. We verified that RAS functions including nucleotide exchange, sensitivity to SoS, and effector binding are preserved in this fusion construct (fig. S12). Our model (Fig. 4A) predicts that this chimera would localize to the PM through a farnesylated HVR under the resting state, whereas elevated Ca^{2+}

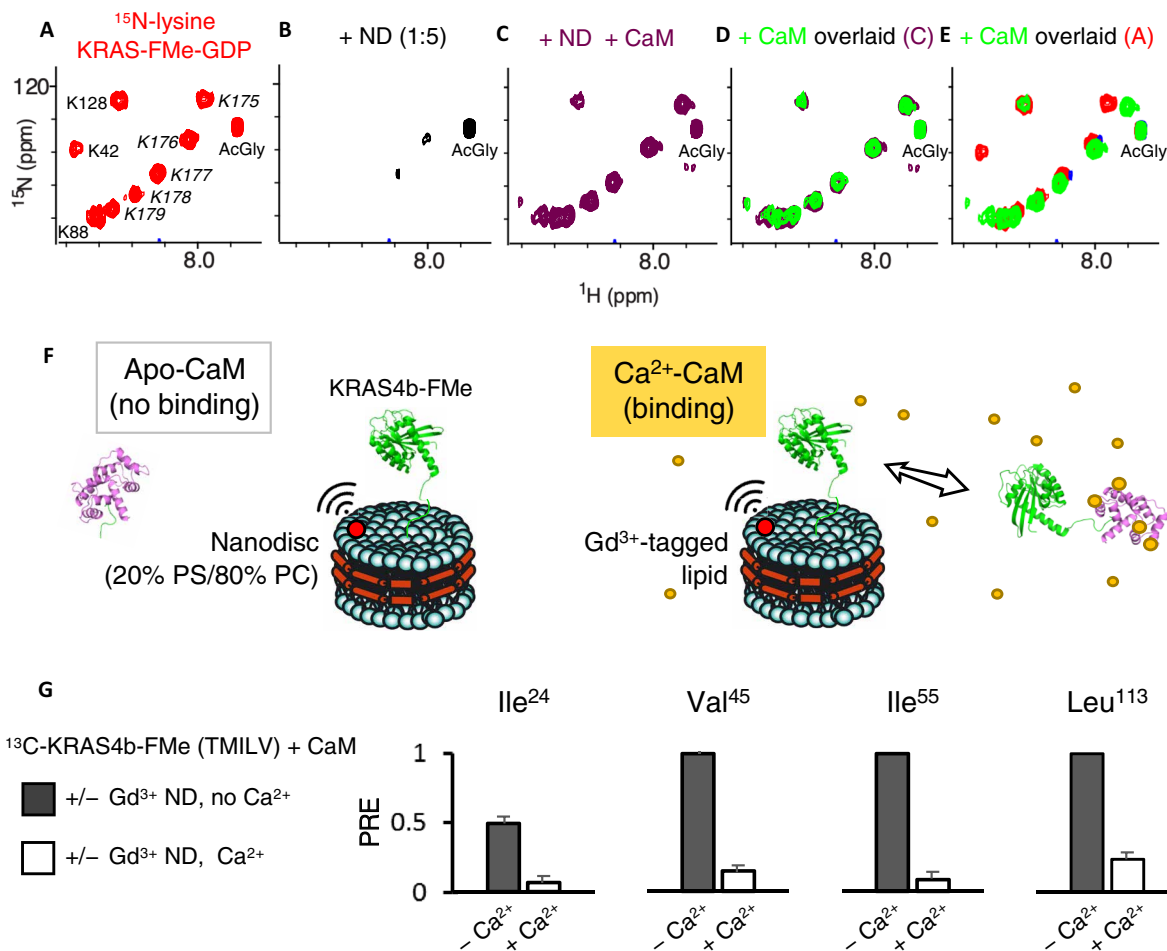


Fig. 3. Alternative isotopic labeling schemes of KRAS4b-FMe show CaM binding is mutually exclusive with membrane association. (A to E) Fully processed KRAS4b-FMe, specifically labeled with ¹⁵N-lysine in insect cells, provides 5 NMR probes in the HVR and 11 probes in the G-domain. The chosen window highlights the lysine residues in the HVR (in italics). Samples contain 20 μM acetyl glycine (AcGly) as an internal standard. Shown are ¹H-¹⁵N HSQC spectra for (A) KRAS4b-FMe alone; (B) KRAS4b-FMe after addition of NDs composed of 80% DOPC and 20% DOPS (fivefold excess KRAS4b-FMe); (C) KRAS4b-FMe in the presence of NDs and Ca²⁺-CaM (1:1 KRAS4b-FMe molar ratio); (D) KRAS4b-FMe and Ca²⁺-CaM in the absence of NDs, overlaid with (C), in the presence of NDs; and (E) KRAS4b-FMe and Ca²⁺-CaM overlaid with (A), KRAS4b-FMe alone. Data are representative of two experiments each. (F) Model of the predicted interactions between KRAS4b-FMe, membranes (NDs), and CaM in the presence and absence of Ca²⁺ using paramagnetic relaxation enhancement (PRE). Without Ca²⁺, KRAS4b-FMe is associated with the membrane through HVR electrostatics and farnesyl insertion and experiences significant peak broadening by membrane embedded PRE-active Gd³⁺. After addition of Ca²⁺ and activation of CaM, KRAS4b-FMe is extracted from the membrane by CaM and is thus unaffected by PRE-broadening at the membrane. (G) Experimentally derived probe peaks for PRE interactions (Ile²⁴, Val⁴⁵, Ile⁵⁵, and Leu¹¹³) within KRAS4b-FMe, specifically methyl-labeled with ¹³C-Thr, Ile, Leu, Val, and Met (TMILV) in an insect cell expression system, in the presence or absence of 5 mM Ca²⁺. A PRE reading of 1 means complete loss of signal, and a reading of 0 signifies no change in peak intensity relative to pre-Ca²⁺. Spectra were normalized by 0.6 mM sodium trimethylsilylpropanesulfonate (DSS) internal standard peak intensities. Error bars represent spectral noise. Data are representative of two experiments.

would lead to binding of the CaM domain to the farnesyl moiety. The structural rearrangement from an unbound state on the membrane to a KRAS4b:CaM interaction in the cytosol would perturb the orientation and proximity of the two fluorophores and potentially alter FRET efficiency. We have named this chimeric construct “CaMeRAS” for its function as a “camera” to probe the CaM and KRAS4b interaction.

To test whether CaMeRAS exhibits a FRET response to changes in Ca²⁺ concentration, a FLAG-CaMeRAS construct was expressed in HeLa cells, purified, and titrated with Ca²⁺ in vitro (fig. S13). CaMeRAS exhibited a small (5.5%) but statistically significant and reliable increase in FRET efficiency in a dose-dependent manner upon addition of Ca²⁺. In vitro Ca²⁺ titrations of a farnesylation-deficient CaMeRAS variant, i.e., KRAS4b-C185Astop (CaMeRAS^{185A}) elicited a small FRET response,

likely induced by compaction of CaM upon binding Ca²⁺. Consistently, a calcium-binding deficient CaMeRAS mutant with an E to Q mutation in each EF hand, i.e., CaM E1234Q [CaMeRAS^{1234Q}, EF1-E31Q, EF2-E67Q, EF3-E104Q, and EF4-E140Q (59, 60)] exhibited no change in FRET in response to Ca²⁺. These data demonstrate that CaMeRAS senses a Ca²⁺- and farnesyl-dependent, specific interaction between KRAS4b-FMe and CaM (Fig. 4B), which is reversible upon chelation of Ca²⁺ by EDTA (Fig. 4C). The maximal FRET drops below the Ca²⁺-free baseline after chelation for both CaMeRAS^{WT} and CaMeRAS^{185A}, likely because there is residual Ca²⁺ in buffers before Ca²⁺ titration. The Ca²⁺-insensitive CaMeRAS^{1234Q} did not exhibit a change upon addition of Ca²⁺ or EDTA. Having developed and validated this FRET construct in vitro, we sought to validate our binding model in vivo.

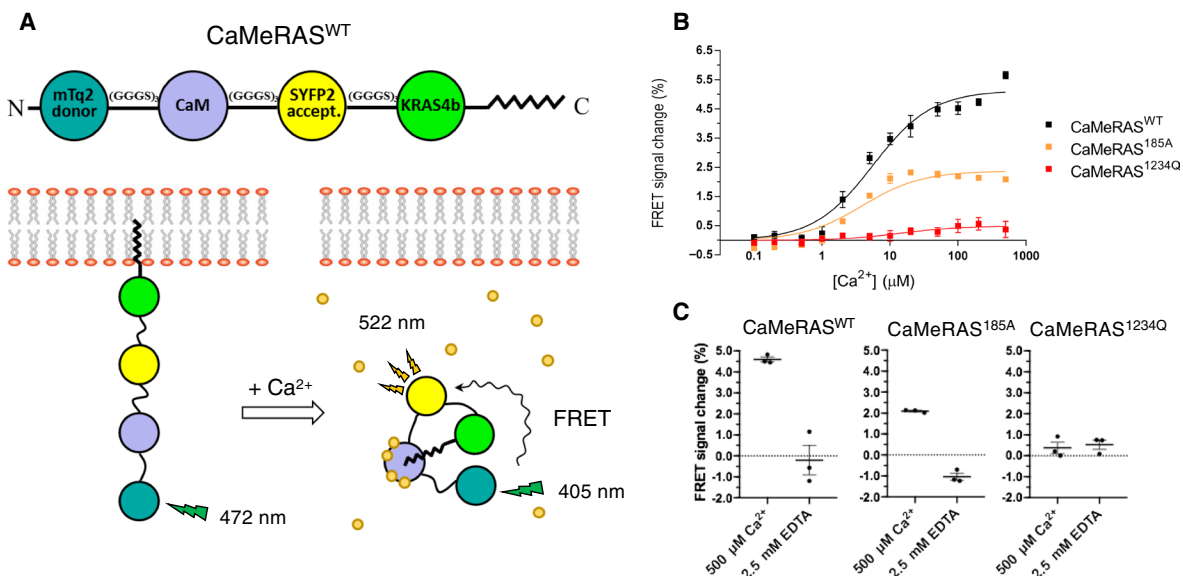


Fig. 4. CaMeRAS FRET construct demonstrates Ca^{2+} - and farnesyl-dependent FRET signal change in vitro. (A) Schematic of chimeric construct expressed in HEK293 and HeLa cells and bimodal use for CaM-KRAS4b binding model validation. When transiently expressed in mammalian cells, the chimeric construct is natively processed at the C-terminal CaaX box, allowing tethering of the construct to the PM. Upon Ca^{2+} influx, Ca^{2+} -CaM extracts KRAS4b from the membrane, visible with fluorescence imaging, and the structural rearrangement of the chimera leads to detectable FRET. (B) FRET signal (SYFP2/mTq2 emission ratio) changes during in vitro Ca^{2+} titration into purified CaMeRAS^{WT} (black) CaMeRAS bearing a mutation that prevents farnesylation (CaMeRAS^{185A}; FLAG-mTq2-CaM-SYFP2-KRAS4b-C185Astop, orange) or mutations that block Ca^{2+} binding (CaMeRAS^{1234Q}; FLAG-mTq2-CaM[E31Q, E67Q, E104Q, E140Q]-SYFP2-KRAS4b, red). Data are presented as means \pm SEM of three independent measurements. FRET signal was calculated by using the peak intensities of mTq2 (at 472 nm) and SYFP2 (at 522 nm) in emission spectra as shown in fig. S12. Data were fit with sigmoidal dose-response equation on Prism8 software (GraphPad). (C) In vitro Ca^{2+} -dependent CaMeRAS FRET changes in the presence of 0.5 mM Ca^{2+} and after addition of 2.5 mM EDTA. CaMeRAS^{WT}, CaMeRAS^{185A}, and CaMeRAS^{1234Q} are described in (B). Data are presented as means \pm SEM of three independent measurements.

Ca^{2+} stimulation induces reversible KRAS4b-FME-CaM interactions and membrane extraction in cells

To fully assess the behavior of the KRAS4b-CaM interaction in mammalian cells, we used live-cell fluorescence imaging using the CaMeRAS constructs (Fig. 5A) transiently expressed in HeLa cells. As expected, the farnesyl-containing constructs CaMeRAS^{WT} and CaMeRAS^{1234Q} were concentrated on the PM in resting cells, with a fraction visible in the cytoplasm or on endomembranes, whereas the non-farnesylated CaMeRAS^{185A} exhibited constitutive cytoplasmic localization (Fig. 5B). Induction of Ca^{2+} influx by addition of the calcium ionophore ionomycin (fig. S14, A and B) or histamine, which produces a physiologically relevant Ca^{2+} cascade, caused rapid relocation of CaMeRAS^{WT} off the PM, consistent with CaM sequestration of the farnesyl moiety (Fig. 5C). CaMeRAS^{1234Q}, which is defective for Ca^{2+} -binding, retained PM localization following Ca^{2+} stimulation, and the cytoplasmic localization of CaMeRAS^{185A} was not affected by Ca^{2+} influx (Fig. 5C). The maintenance of PM localization of CaMeRAS^{1234Q} after Ca^{2+} influx indicates that the observed internalization of CaMeRAS^{WT} is not due to charge-shielding effects of Ca^{2+} ions at the PM. Representative graphs of CaMeRAS construct localization over time, based on the fluorescence intensity of mTq2 in line-scan cross sections of HeLa cells after histamine stimulation (Fig. 5D), illustrate time-dependent translocation of CaMeRAS^{WT} from the PM to the cytoplasm in response to histamine.

Having demonstrated the Ca^{2+} -induced translocation of CaMeRAS^{WT} in live cells, we sought to further examine whether this phenomenon is synchronized with Ca^{2+} signaling and how translocation may be coupled to the Ca^{2+} -dependent FRET change observed in vitro.

Using Calbryte 630, a fluorescent Ca^{2+} indicator with an absorbance spectrum discrete from mTq2 and SYFP2, we were able to extend our in-cell fluorescence system to simultaneously coimage Ca^{2+} , mTq2, and SYFP2 in response to histamine stimulation. Imaging mTq2 confirmed the CaMeRAS localization and translocation described above (Fig. 6A), whereas concurrent Ca^{2+} imaging showed a cytosolic increase of Ca^{2+} after histamine stimulation of these HeLa cells (Fig. 6B). In cells expressing CaMeRAS^{WT}, histamine stimulation produced a large and sustained Ca^{2+} signal, possibly amplified by interactions between CaM and ion channels on the membrane, which was reversible with the addition of the cell permeable Ca^{2+} chelator BAPTA-AM. Cells expressing CaMeRAS^{185A} or CaMeRAS^{1234Q} exhibited a more physiological Ca^{2+} response to histamine, possibly due to lack of membrane localization or Ca^{2+} binding, respectively. Segmenting the images into PM and cytosolic areas to assess localization showed internalization of CaMeRAS^{WT}, which was reversible with the addition of BAPTA-AM, whereas CaMeRAS^{185A} retained cytoplasmic localization and CaMeRAS^{1234Q} remained localized on the membrane (Fig. 6C), consistent with our previous results.

In the same cells, FRET was measured by comparing the ratio of mTq2 to SYFP2 within many small segments along the PM and in the cytoplasm, before and after histamine stimulation (fig. S15A). Peak FRET values taken from Gaussian-modeled histograms of these data showed that CaMeRAS^{WT} exhibited a 7% reversible FRET increase upon Ca^{2+} -induced translocation from the membrane to the cytoplasm (Fig. 6D and fig. S15B). A minor (<2%) FRET change was observed in the cytosol for CaMeRAS^{185A}, consistent with our in vitro titration data, likely due to the conformational change of CaM in

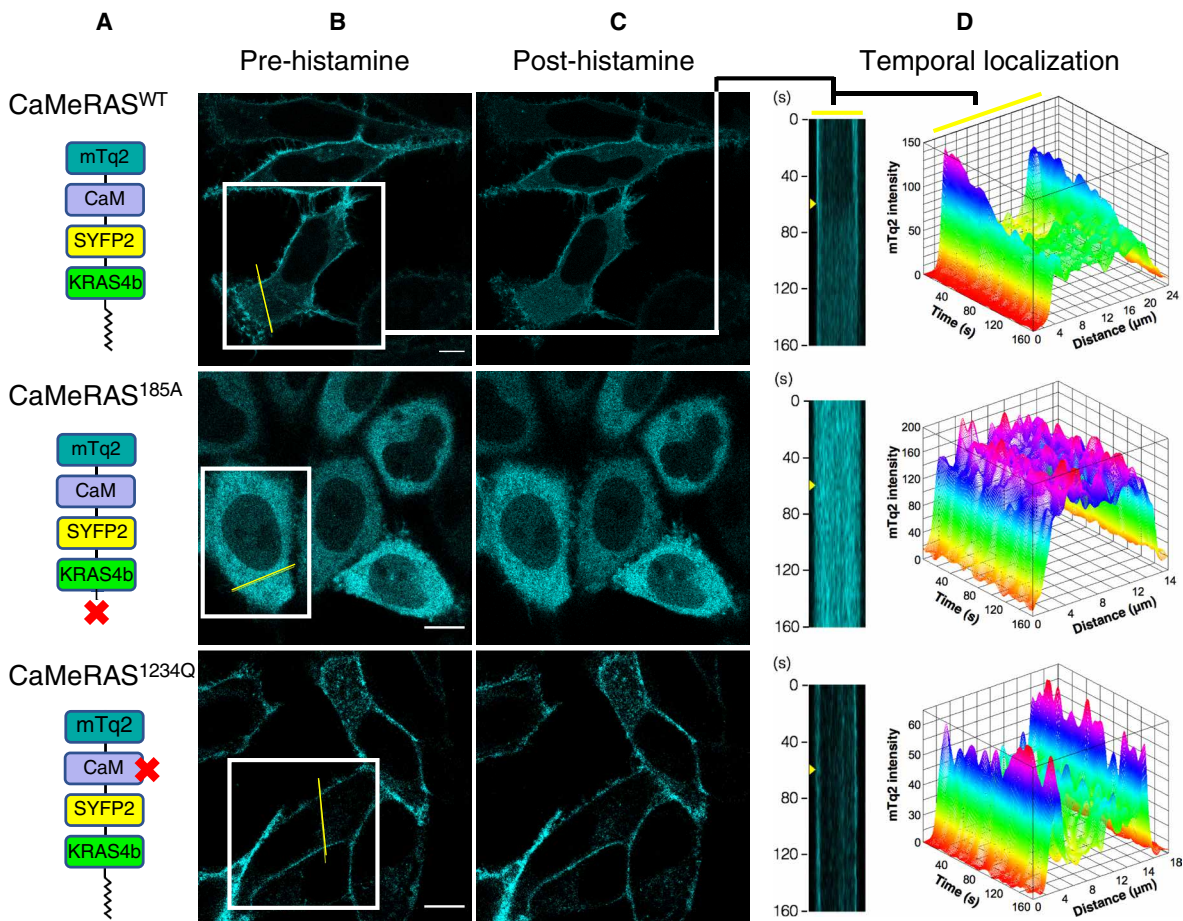


Fig. 5. Tracking cellular localization of CaMeRAS constructs in HeLa cells following histamine stimulation. (A) Schematic of CaMeRAS constructs transiently expressed (CaMeRAS^{WT}, CaMeRAS^{185A}, and CaMeRAS^{1234Q}), with a red "X" indicating where the mutants are deficient. The farnesyl moiety is represented by the zig-zag line. (B to D) Live-cell imaging tracking the cellular localization (mTq2) of constructs before (B) and 60 s after (C) 100 μ M histamine stimulation. Panel (D) shows representative mTq2 intensity distributions at the indicated cross sections (yellow lines in (B)) over time, from 0 s [as shown in (B)] to 160 s; the 120-s time point is as shown in (C); histamine was added at 60 s (yellow arrowheads) after starting imaging. Scale bars, 10 μ m. Data are representative of five experiments, each analyzing five to six cells.

response to Ca^{2+} binding. No detectable FRET change was observed on the PM for CaMeRAS^{1234Q} (Fig. 6D and fig. S15C). Statistics for the FRET histogram analyses are summarized in tables S1 and S2, and videos show each CaMeRAS construct's response to histamine stimulation (Ca^{2+} , mTq2, and SYFP2 coimaging) (movies S1 to S5). To further validate the observed *in vivo* FRET, the CaMeRAS were visualized under the same conditions using fluorescence-lifetime imaging, a sensitive measure of the rate at which excited fluorophores decay to their ground states, which is affected by changes in structure, dynamics, and fluorescent energy transfer. After histamine stimulation, the cytoplasmic CaMeRAS^{WT} displayed a statistically significant decrease in fluorescence lifetime relative to the membrane-localized protein before stimulation (fig. S16). The reduction in fluorescence lifetime, indicative of a change in distance and relative orientation between mTq2 and SYFP2, combined with the reversible internalization of the sensor, strongly supports our model of Ca^{2+} -dependent sequestration of KRAS4b farnesyl by CaM, which outcompetes PM binding. Stimulation of HEK293 cells with 100 μ M adenosine 5'-triphosphate (ATP) to elicit a Ca^{2+} signal produced similar results (fig. S17), confirming the robustness of the Ca^{2+} -dependent translocation of CaMeRAS.

DISCUSSION

The interaction between KRAS4b and CaM has been studied for decades, with increasing intensity in recent years as therapeutic potential was recognized. However, many of the reported details of the interaction have been inconsistent. Here, we combined biophysical studies on fully processed full-length KRAS4b with observations of an engineered biosensor in live cells and demonstrated a Ca^{2+} -dependent, nucleotide-independent interaction mediated by hydrophobic sequestration of the KRAS4b farnesyl moiety within the CaM C-lobe. This interaction directly competes with membrane association and causes relocalization of KRAS4b within cells. Our atomic-resolution structure of Ca^{2+} -CaM complexed with the farnesyl cysteine moiety revealed intimate interactions between the hydrophobic acyl chain and hydrophobic residues of the C-terminal lobe (Phe⁹², Ile¹⁰⁰, Leu¹⁰⁵, Met¹⁰⁹, Met¹²⁴, Ile¹²⁵, Ala¹²⁸, Val¹³⁶, Phe¹⁴¹, and Met¹⁴⁴). Using this structure, we designed the biosensor CaMeRAS, which enabled visualization of Ca^{2+} -dependent, reversible translocation of KRAS4b from the PM to the cytoplasm in HeLa and HEK293 cells, supporting the notion that canonical plasma membrane KRAS4b signaling is dampened by Ca^{2+} -CaM. Furthermore, this competition between membrane anchoring and CaM binding only occurs upon elevation of cytoplasmic Ca^{2+} concentrations.

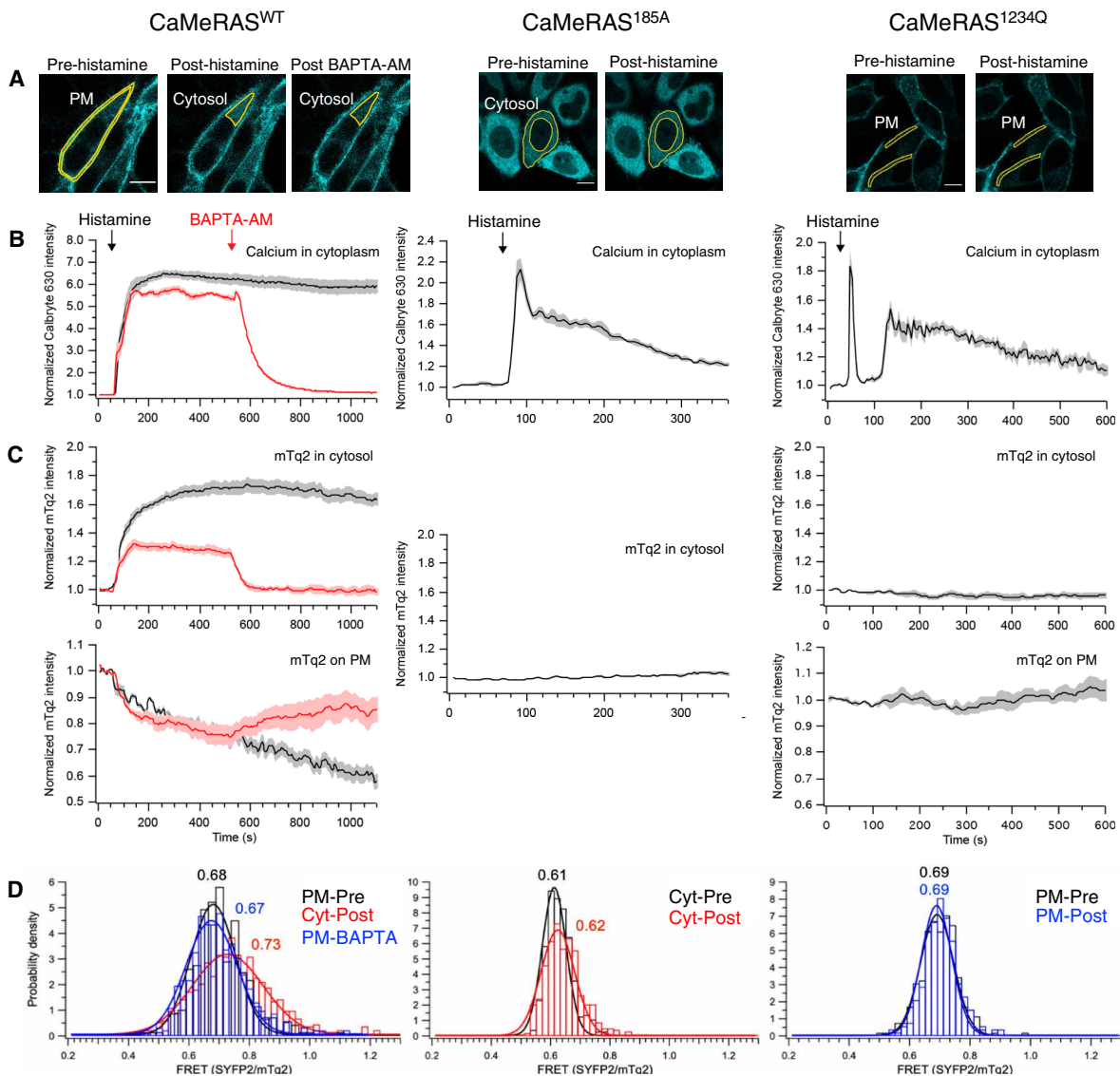


Fig. 6. CaMeRAS demonstrates reversible Ca^{2+} -farnesyl-dependent internalization and FRET change in live cells. (A) Cellular localization (mTq2) of CaMeRAS constructs in HeLa cells before and after 100 μM histamine stimulation. BAPTA-AM (10 μM) treatment was added to HeLa cells expressing CaMeRAS^{WT} to examine reversibility. Regions of interest on the PM or in the cytosol were drawn manually as shown with white outlines. Data are representative of five experiments, each analyzing 5 to 10 cells. (B and C) In the cells described in (A), cytoplasmic Ca^{2+} concentration [assessed as normalized Calbryte 630 intensity tracking; (B)] and cytoplasmic and PM localization of CaMeRAS constructs (C) were traced over time after histamine stimulation and, for CaMeRAS^{WT} cells, BAPTA-AM treatment (red trace). In these traces, the bold lines denote the mean, and the shadows represent the SEM from five independent cells pooled from a single representative experiment. (D) Histograms of FRET readouts (ratio of SYFP2/mTq2 emissions) of the localization of CaMeRAS constructs [as aligned under (A)] at the PM and cytoplasm before (Cyt-Pre) and after (Cyt-Post) histamine stimulation (and for the WT construct, BAPTA-AM; “BAPTA”) in the marked regions of interest (see fig. S14). Data fitting of the normal distributions was performed using Gaussian functions, and data were pooled from 15 to 20 cells across three independent experiments.

Sequestration of KRAS4b farnesyl in the CaM C-lobe hydrophobic pocket forms the “core” of the KRAS4b–CaM interaction, which is likely further stabilized by electrostatic contacts between the KRAS4b HVR and the acidic CaM surface. However, previous biophysical studies demonstrated that isolated CaM N- and C-lobes are each capable of binding KRAS4b-FME, with the C-lobe exhibiting three- to eightfold higher affinity (40), consistent with our finding that CaM mutants with N- or C-lobe Ca^{2+} -binding deficiencies still bind farnesyl-derived compounds through the intact lobe. The higher-affinity C-lobe binding has also been predicted by molecular dynamics studies

of the farnesylated KRAS4b HVR in complex with CaM (39, 61). Among many models, the two highest confidence interaction modes involved the farnesyl group buried deeply within either the N-lobe or C-lobe hydrophobic pocket and electrostatic interactions between the KRAS4b polybasic region and the surface of CaM. The C-lobe binding model is markedly similar to our crystal structure and has nearly twice the calculated binding free energy of the N-lobe binding model (39), consistent with biophysical results (40). Despite this difference in affinities, a 2:1 stoichiometry for the interaction of KRAS4b-FME with intact CaM has been reported, which is reduced to 1:1 with the

truncation of CaM N- or C-lobes (40). We believe that our crystal structure exhibits exclusive C-lobe binding primarily due to its higher affinity and the FCME concentration used in crystallization, whereas 2:1 binding becomes feasible under more saturating conditions.

An analogous CaM-lipoprotein interaction was previously observed in a crystal structure of N-terminally myristoylated polybasic peptide (CAP23/NAP22) in complex with CaM, in which the myristoyl was sequestered within the hydrophobic core (PDB: 1L7Z) (49). This CaM-myristoyl complex somewhat resembles our CaM-farnesyl structure, but there are two significant differences: (i) the orientation of the lipid within the hydrophobic core and (ii) the position of $\alpha 4$ (fig. S8A). The myristoyl group is found in a linear orientation, interacting with hydrophobic surfaces of both lobes, but not deeply inserted in the pockets, whereas FCME is bound in the C-lobe pocket only, with the N-lobe pocket minimally exposed (fig. S8B). These differences likely stem from the unsaturated and branched farnesyl moiety being shorter and bulkier than myristoyl. In our CaM:FCME complex, the farnesyl moiety adopts a bent conformation, similar to that observed with PEX19 (62) and aristolochene synthase but differing from the extended conformations observed with farnesyltransferase (63) and PDE δ (64). The C-terminal cysteine residue occupies a position equivalent to that of the N-terminal myristoylated glycine in CAP23/NAP22, thus tethering their adjacent polybasic sequences in the same region, albeit with opposite strand directions.

The myristoyl/farnesyl-bound CaM conformations are distinct from CaM in complex with canonical peptides but are remarkably similar to CaM in complex with the unusual target myristoylated alanine-rich C-kinase substrate (MARCKS) (PDB: 1IWQ). This internal MARCKS peptide, which is not myristoylated, assumes an extended conformation with a short helix presenting a Phe side chain that is buried deeply in the C-lobe and a Leu two residues away that contacts a closed N-lobe (65).

CaM interactions with other myristoylated polybasic peptides similar to CAP23/NAP22, namely, the vSRC N-terminal peptide pp60v and the HIV1 Nef1 peptide, were also previously studied by NMR (45, 46). Additions of these peptides to ^{15}N -CaM induced CSPs extremely similar to those induced by FCME (fig. S3). Other small GTPases with geranylgeranylated C-terminal polybasic sequences have also been reported to interact with CaM (21, 66–68), suggesting that singly lipidated, terminal polybasic sequences may represent a general noncanonical CaM-binding motif.

Unlike KRAS4b, the HRAS, NRAS, and KRAS4a isoforms are all subject to enzymatic cycles of palmitoylation/depalmitoylation, which modulate affinity for the membrane and control signal output (69–71). The high affinity of these isoforms for the membrane, C-terminal bulkiness, and minimal charge all likely contribute to their incompatibility with CaM binding. KRAS4b and other GTPases that lack regulated palmitoylation may have evolved other cellular mechanisms to regulate membrane attachment and signal output. We believe that CaM serves this vital role in response to Ca^{2+} signaling, and the chimeric FRET construct CaMeRAS offers a glimpse at this regulation in vivo.

In addition to the Ca^{2+} -dependent internalization of KRAS4b by CaM, which abrogates canonical KRAS4b signaling, there are other postulated consequences of this interaction, including the sequestration of Ca^{2+} -bound CaM by KRAS4b, which reduces CaMKII activation and suppresses noncanonical Wnt/ Ca^{2+} signaling, thereby promoting tumorigenicity (22). Furthermore, relocalization of KRAS4b to endomembranes may enable interactions with other proteins, such as Bcl-XL, which occurs upon relocalization of KRAS4b to mitochondria in response to phosphorylation of Ser¹⁸¹ by protein kinase C (25–27).

These reports also demonstrate that phosphorylation at Ser¹⁸¹ and CaM binding are mutually exclusive, hinting at a signal-dependent interplay between multiple regulatory mechanisms (25). The direct and ill-defined competition between CaM binding, phosphorylation, and PDE δ cycling, which returns internalized KRAS4b to the PM from endosomes (18, 64), indicates the existence of a complex regulatory network. PDE δ and CaM would compete for binding to the farnesyl group of KRAS4b: CaM exhibits ~5-fold higher affinity (40, 64), but its interaction is spatiotemporally limited to a Ca^{2+} signaling event.

Collectively, our data provide new insights into the regulation of KRAS4b by CaM, supply tools for this growing field, and solidify the farnesyl-dependent membrane extraction and relocalization paradigm for this interaction. Rigorous biophysical studies of Ca^{2+} -CaM regulation of KRAS4b and the cross-talk between MAPK and Ca^{2+} signaling lead to approaches to exploit this interaction for new therapeutic avenues.

MATERIALS AND METHODS

Bacterial protein expression and purification (CaM/KRAS 1–185/BRAF RBD/SoS_{cat})

E. coli BL21 CodonPlus cells were transformed with pET28 plasmids containing CaM or KRAS4b sequences and grown at 37°C to an optical density of 0.6 to 0.8. Temperature was reduced to 15°C before induction of protein expression with 0.25 mM isopropyl- β -D-thiogalactopyranoside. Cells were grown in Luria-Bertani media with 1 mM kanamycin for unlabeled protein production or M9 [biotin (1 mg/liter), thiamine (1 mg/liter), 0.3 mM CaCl_2 , 1 mM kanamycin, 0.2% (w/v) glucose, trace elements (25 μM EDTA, 30.83 μM ferric chloride, 3.67 μM zinc chloride, 0.74 μM cupric chloride, 0.42 μM cobalt chloride, 1.62 μM boric acid, and 127.19 μM manganese chloride), and ^{15}N - NH_4Cl (1 g/liter)] for uniform ^{15}N labeling. Cells were lysed by sonication in buffer containing 50 mM tris-HCl (pH 8), 150 mM NaCl, 0.1% (v/v) NP-40, 10% (v/v) glycerol, 10 mM imidazole, 5 mM MgCl_2 , 10 mM β -mercaptoethanol, 1 mM phenylmethylsulfonyl fluoride, lysozyme, and deoxyribonuclease. CaM and unprocessed KRAS were purified by Ni-nitrilotriacetic acid His-tag affinity chromatography followed by gel filtration. A thorough purification protocol can be found here (72). N-terminally glutathione S-transferase (GST)-tagged B-Raf proto-oncogene serine/threonine kinase (BRAF) RAS-binding domain (RBD, residues 150 to 233) and His-tagged catalytic domain of SoS (SoS_{cat}, residues 564 to 1049) were cloned into pGEX-4T2 (GE Healthcare) and pET15b (Novagen/EMD Biosciences), respectively, expressed in *E. coli* BL21 (DE3), and purified as previously described (73).

Insect cell culture (isotope labeling)

High Five insect cells (Thermo Fisher Scientific) were transfected with bacmids containing farnesyl transferases 1 and 2 and His-MBP (maltose-binding protein)-KRAS4b (gift from NCI Frederick). Expression and purification of these constructs followed a previously reported protocol (44). ^{15}N -lysine labeling of KRAS4b was performed in ESF 921 Delta Series media (ΔKRWYFH) (Expression Systems) supplemented with Arg (800 mg/liter), Trp (200 mg/liter), Tyr (360 mg/liter), Phe (1000 mg/liter), and His (200 mg/liter) (Sigma-Aldrich). ^{15}N -lysine (Cambridge Isotope Laboratory) was added (100 mg/liter) 16 hours after infection. ^{13}C -methyl labeling of KRAS4b was performed in ESF 921 Delta Series media (ΔTMILVA) supplemented with Ala (400 mg/liter). ^{13}C -methyl-labeled Thr (75 mg/liter),

Met (100 mg/liter), Ile (150 mg/liter), Leu (100 mg/liter), and Val (50 mg/liter) were added 16 hours after infection based on a protocol adapted from Gossert *et al.* (74, 75).

¹H-¹⁵N HSQCs

Samples were prepared for NMR by mixing the appropriate labeled proteins and substrates in NMR buffer containing 50 mM Hepes (pH 7.4), 100 mM NaCl, 1 mM tris(2-carboxyethyl)phosphine (TCEP) and 10% D₂O. Most experiments also included 5 mM MgCl₂ and/or 10 mM CaCl₂. NMR experiments were primarily conducted on a 600-MHz Bruker Avance magnet with 1.7-mm cryoprobe and 40 μl of sample volumes. Experiments conducted on an 800-MHz magnet had 450 μl of samples in 5-mm tubes.

NMR titrations

(E,E)-farnesol, (Z,Z)-farnesol, and (Z,Z)-FCME were solubilized in DMSO to 100 mM, appropriately diluted in NMR buffer, and added directly to separate NMR samples to a final concentration of 2.5% DMSO. Titration HSQCs were collected with 216 μM CaM and 0-, 0.35-, 0.7-, 1-, 1.4-, 2.9-, 5.8-, 11.5-, 14.3-, and 29-fold excess farnesyl compound in an autosampler connected to a 600-MHz Bruker Avance magnet at 25°C. KRAS4b-FMe titrations were collected at 0.1-, 0.4-, 0.8-, 1-, 1.3-, 2-, and 4-fold excess over 0.1 mM CaM under the same conditions.

Crystallization/structure determination

CaM [1 mM; 20 mM Hepes (pH 7.4) and 10 mM Ca²⁺] was screened for crystallization with 5 mM FCME at room temperature using Protein Complex (Qiagen), Wizard Classic (Rigaku), and Crystal Screen HT (Hampton Research) commercial screening kits. A successful condition from Crystal Screen HT containing 0.2 mM ammonium acetate, 0.1 mM sodium cacodylate (pH 6.5), and 30% (w/v) polyethylene glycol (PEG) 8000 was further optimized for pH and PEG concentration with 1 and 1.25 mM CaM. The diffracted crystal was grown in 5 mM FCME, 0.2 mM sodium acetate, 0.1 mM sodium cacodylate (pH 6.7), and 28% PEG 8000, with 1.25 mM CaM. Glycerol was used as a cryoprotectant. Diffraction data from the Canadian Macromolecular Crystallography Facility 08ID-1 Beamline at the Canadian Light Source were processed with HKL2000 (76) and modeled and refined using COOT (77) and Phenix (78).

ND preparation

All lipids were purchased from Avanti Polar Lipids, Inc. NDs were prepared according to previous protocols (55). 1,2-distearoyl-*sn*-glycero-3-phosphoethanolamine-*N*-diethylenetriaminepentaacetic acid (gadolinium salt) [PE-DTPA(Gd³⁺)] was added to the lipids at a molar ratio of 20 DOPC:5 DOPS:1 PE-DTPA (Gd³⁺). The organic solvents were then removed using gentle nitrogen flow followed by vacuum, and the dried lipid film was solubilized in aqueous buffer containing detergent [20 mM tris (pH 7.4), 100 mM NaCl, and 100 mM sodium cholate]. This mixture was subjected to three freeze/thaw cycles and vortexed until clarified, and then membrane scaffold protein [MSP1D1, prepared as described previously (79)] was added at a 1:40 molar ratio relative to the lipids. After 1-hour incubation with mild rotation at 20°C, sodium cholate was removed from the MSP-lipid mixture with Bio-Beads SM-2 adsorbents (Bio-Rad) using a batch method with 2-hour incubation at room temperature with mild rotation. The ND particles were then purified via size exclusion chromatography using a 26/60 Superdex 200 column equilibrated with buffer A without TCEP. The particle size was analyzed

with dynamic light scattering and corresponded with a 10-nm-diameter particle.

ND-binding PRE

Baseline ¹H-¹³C HSQC spectra of 200 μM ¹³C-TILVM KRAS4b-FMe were collected on a 600-MHz Bruker Avance magnet in the presence and absence of unlabeled CaM, with and without Ca²⁺, at 25°C. PRE experiments were initiated by the addition of 1:20 molar ratio Gd³⁺-containing ND to similarly prepared NMR samples and collecting corresponding HSQCs. Peak intensity ratios were calculated for ND versus baseline for CaM-containing samples, either in the presence of Ca²⁺ [20 mM Hepes (pH 7.3), 100 mM NaCl, 1 mM TCEP, 5 mM Mg²⁺, and 5 mM Ca²⁺] or absence of Ca²⁺ [20 mM Hepes (pH 7.3), 100 mM NaCl, 1 mM TCEP, and 0.5 mM Mg²⁺] by normalizing intensities to a 0.6 mM sodium trimethylsilylpropanesulfonate internal standard.

Plasmid constructions for FRET chimeras

The plasmid containing a codon-optimized KRAS4b (KRAS4b-opt) was purchased from Invitrogen GeneArt Gene Synthesis (Thermo Fisher Scientific). pmTurquoise2-C1 (80) and pSYFP2-C1 (81) were gifts from D. Gadella (Addgene plasmid nos. 60560 and 22878, respectively). pEZYmyc-His (82) was a gift from Y.-Z. Zhang (Addgene plasmid no. 18701). A complementary DNA (cDNA) encoding KRAS4b-opt amplified by polymerase chain reaction (PCR) was cloned into pENTR1A (Invitrogen) between Bam HI and Not I sites (plasmid #1). Then, a cDNA encoding CaM amplified by PCR was cloned into Bam HI site of plasmid #1 (plasmid #2). Furthermore, to insert mTq2 and SYFP2 into plasmid #2, two short linkers including restriction enzyme site(s) were inserted at the 5'-end of CaM and between CaM and KRAS4b-opt using Q5 site-directed mutagenesis (New England Biolabs Inc.) (plasmid #3). Then, cDNAs of mTq2 and SYFP2 amplified by PCR using pmTurquoise2-C1 and pSYFP2-C1 as templates were cloned into Sph I and Kpn I sites and Spe I and Bam HI sites of plasmid #3, respectively, producing mTq2-CaM-SYFP2-KRAS4b, identified as CaMeRAS^{WT}. For making a construct of mTq2-CaM1234Q-SYFP2-KRAS4b, called CaMeRAS^{1234Q}, a cDNA of CaM1234Q (E31Q, E67Q, E104Q, and E140Q) amplified by PCR was used to replace wild-type CaM. For mTq2-CaM-SYFP2-KRAS4b-Cys185Astop or CaMeRAS^{185A}, Cys¹⁸⁵ in KRAS4b was mutated to Ala, and TAA stop codon was inserted after Ala using Q5 site-directed mutagenesis. To insert FLAG tag at the N terminus, a cDNA encoding FLAG-mTq2 was amplified by PCR using a forward primer harboring a FLAG sequence at the 5'-end and replaced with nontagged mTq2. mTq2-CaM-SYFP2-KRAS4b and mutants made in pENTR1A were transferred into pEZYmyc-His by Gateway LR Clonase II (Invitrogen). All plasmids were confirmed by DNA sequencing. The sequences of all primers used (table S3) and the full amino acid sequence for the chimeric construct (fig. S18) are provided in the Supplementary Materials.

Expression and purification of FLAG-mTq2-CaM-SYFP2-KRAS4b and mutants

HeLa cells were transfected with plasmids containing FLAG-mTq2-CaM-SYFP2-KRAS4b and mutants using a transfection reagent, jetPRIME (Polyplus-transfection). Cells were harvested at ~48 hours after transfection. For purification, cells were resuspended with lysis buffer [50 mM tris, 300 mM NaCl, 2 mM dithiothreitol (DTT), and 1 mM EDTA (pH 7.4) supplemented with cOMplete EDTA-free protease inhibitor cocktail (Roche)] and lysed using an EmulsiFlex-C3

(Avestin). Cell lysate was centrifuged at 45,000g for 30 min to remove cell debris. The supernatant was loaded to anti-FLAG M2 agarose (Sigma-Aldrich) and washed with the same buffer for lysis. FLAG-mTq2-CaM-SYFP2-KRAS4b was eluted with 3×FLAG peptide (0.15 mg/ml; APExBIO) in the buffer [50 mM tris, 300 mM NaCl, and 2 mM DTT (pH 7.4)].

In vitro FRET-based calcium titration

Purified FLAG-mTq2-CaM-SYFP2-KRAS4b was dialyzed with the buffer [50 mM tris, 300 mM NaCl, and 2 mM DTT (pH 7.4)] in which residual calcium had been chelated with Chelex 100 resin (Bio-Rad). Fluorescence measurement was made on a Shimadzu RF-5301PC fluorimeter (Shimadzu Corp.), and emission spectra of FLAG-mTq2-CaM-SYFP2-KRAS4b excited by 405-nm light in the presence of various concentrations of CaCl₂ were scanned from 420 to 600 nm at 20°C.

Biolayer interferometry

We investigated effector binding, intrinsic nucleotide exchange, and SoS_{cat}-dependent nucleotide exchange of the CaMeRAS fusion protein using an Octet RED 384 biolayer interferometry instrument equipped with the Octet Data Acquisition 9.0.0.37 software (Pall FortéBio). Initially, GST-BRAF-RBD was immobilized to anti-GST-conjugated biosensors (Pall FortéBio) by incubating the sensor in a well containing GST-BRAF-RBD (5 µg/ml) for 10 min. To test the intrinsic exchange of CaMeRAS, we incubated 1.5 µM purified protein and 10 mM GTPγS in a 96-well plate. The impact of SoS_{cat} on the nucleotide exchange was assessed by addition of SoS_{cat} (1:600 molar ratio) to 1.5 µM CaMeRAS and 10 mM GTPγS. In both cases, nucleotide exchange was assessed by immersing the BRAF-RBD-conjugated sensors into the wells containing CaMeRAS at different time intervals. The time-dependent enhancements of the BLI signal induced by CaMeRAS binding the RBD indicated that nucleotide exchange occurred. All proteins were reconstituted in 20 mM Hepes buffer (pH 7.4) containing 100 mM NaCl, 2 mM MgCl₂, 1 mM TCEP, 0.01% BSA, and 0.005% Tween-20. The data were analyzed with FortéBio Data analysis software (Pall FortéBio). Sensors dipped into wells containing 1.5 µM CaMeRAS supplemented with 10 mM GDP were used as a reference.

FRET and calcium imaging and data analysis

HeLa or HEK293 cells were transfected with plasmids containing the mTq2-CaM-SYFP2-KRAS4b or its mutants using jetPRIME (Polyplus-transfection). The cells were subjected to imaging at 18 to 24 hours after transfection. Hank's balanced salt solution (Gibco) supplemented with 1 mM CaCl₂, 0.5 mM MgCl₂, and 0.5 mM MgSO₄ was used as an imaging buffer. After loading the cells with 10 µM Calbryte 630AM (AAT Bioquest), imaging was performed at room temperature using a Leica SP8 confocal microscope with a 63×/1.4 numerical aperture (NA) oil immersion objective lens and high-sensitivity HyD detectors. For simultaneous visualization of mTq2, SYFP2, and Calbryte 630, a 440-nm solid state laser and a white light laser tuned to 608 nm were used for excitation, and fluorescence emission was collected at 455 to 490 nm, 525 to 560 nm, and 620 to 750 nm, respectively. Images were acquired at 3.4 to 4.0 s per frame. Regions of interest on the PM or in the cytosol were selected for mTq2 or SYFP2 fluorescence measurement (Fig. 6A and fig. S15), and quantification was performed using Fiji software (83). Histogram analysis and Gaussian distribution fitting were done using Igor Pro 8 (WaveMetrics Inc.).

Fluorescence lifetime imaging microscopy and data analysis

Fluorescence lifetime images were acquired using a Leica SP8 confocal microscope equipped with a time-correlated single-photon counting module (PicoHarp 300, PicoQuant). The donor (mTq2) was excited using a 405-nm solid-state laser pulsed at a 40-MHz repetition frequency. Fluorescence signal in the emission range of 455 to 480 nm was collected through a 63×/1.4 NA oil immersion objective lens using a cooled single-photon counting HyD SMD detector. Fluorescence lifetime traces were analyzed by using SymPhoTime 64 software (PicoQuant). Statistical difference between pre- and post-histamine stimulation was analyzed by using Wilcoxon signed-rank test.

SUPPLEMENTARY MATERIALS

stke.sciencemag.org/cgi/content/full/13/625/eaaz0344/DC1

Fig. S1. RAS isoform-specific HVRs.

Fig. S2. There is no major interaction between unfarnesylated KRAS4b (1–185) and CaM, independent of bound nucleotide.

Fig. S3. A new class of noncanonical CaM binding targets: Singly lipidated polybasic peptides.

Fig. S4. Chemical shift analysis of CaM residues upon farnesol binding.

Fig. S5. Farnesol and CaM do not interact in the absence of Ca²⁺.

Fig. S6. Farnesyl compound titrations into CaM.

Fig. S7. KRAS4b-FME and farnesol perturbations of ¹⁵N-CaM share a characteristic pattern.

Fig. S8. Structure comparison of CaM conformations bound to FCME and CAP23/NAP22 polybasic myristoylated peptide.

Fig. S9. Lipid orientation in CaM:FCME complex structure.

Fig. S10. Solution NMR PRE validation of CaM-FCME crystal structure.

Fig. S11. Membrane-based PRE probe for KRAS4b-FME interaction with CaM in solution.

Fig. S12. KRAS4b retains function in the CaMeRAS chimera.

Fig. S13. Calcium-dependent change in emission spectra of CaMeRAS chimera FRET protein.

Fig. S14. Tracking cellular localization of CaMeRAS^{WT} in HeLa cells after ionomycin treatment.

Fig. S15. Cellular image segmentation for FRET histogram analysis by Gaussian modeling.

Fig. S16. Fluorescence lifetime of mTq2 of CaMeRAS^{WT} is reduced by histamine stimulation in HeLa cells.

Fig. S17. ATP-evoked Ca²⁺ signal induces CaMeRAS^{WT} internalization and FRET change in HEK293 cells.

Fig. S18. The nucleotide and amino acid sequences of CaMeRAS^{WT} chimeric FRET construct.

Table S1. Peak values of FRET histograms and the numbers of the ROIs analyzed.

Table S2. *P* values from Student's *t* tests comparing Gaussian curve models of FRET histogram data.

Table S3. Primer sequences used for plasmid construction.

Movie S1. Co-imaging CaMeRAS^{WT} and calcium response to histamine stimulation in HeLa cells.

Movie S2. Slow motion highlight: Co-imaging CaMeRAS^{WT} and calcium response to histamine stimulation in HeLa cells.

Movie S3. Coimaging CaMeRAS^{WT} and calcium response to histamine stimulation in HeLa cells and calcium chelation.

Movie S4. Coimaging CaMeRAS^{185A} and calcium response to histamine stimulation in HeLa cells.

Movie S5. Coimaging CaMeRAS^{1234Q} and calcium response to histamine stimulation in HeLa cells.

Data file S1. CaM-farnesol binding CSP by residue.

Data file S2. CaM-FCME PRE.

Data file S3. KRAS4b-ND PRE.

Data file S4. In vitro CaMeRAS Ca²⁺ titration.

Data file S5. Relative fluorophore intensity in vitro as a function of Ca²⁺ titration for CaMeRAS.

Data file S6. In vivo FRET from CaMeRAS constructs in response to histamine stimulation and Ca²⁺ influx.

[View/request a protocol for this paper from Bio-protocol.](#)

REFERENCES AND NOTES

1. M. Barbacid, ras genes. *Annu. Rev. Biochem.* **56**, 779–827 (1987).
2. J. F. Hancock, Ras proteins: Different signals from different locations. *Nat. Rev. Mol. Cell Biol.* **4**, 373–384 (2003).
3. A. G. Stephen, D. Esposito, R. K. Bagni, F. McCormick, Dragging Ras back in the ring. *Cancer Cell* **25**, 272–281 (2014).
4. D. K. Simanshu, D. V. Nissley, F. McCormick, RAS proteins and their regulators in human disease. *Cell* **170**, 17–33 (2017).

5. T. Joneson, D. Bar-Sagi, Ras effectors and their role in mitogenesis and oncogenesis. *J. Mol. Med. (Berl)* **75**, 587–593 (1997).
6. J. L. Bos, ras oncogenes in human cancer: A review. *Cancer Res.* **49**, 4682–4689 (1989).
7. K. L. Bryant, J. D. Mancias, A. C. Kimmelman, C. J. Der, KRAS: Feeding pancreatic cancer proliferation. *Trends Biochem. Sci.* **39**, 91–100 (2014).
8. I. A. Prior, P. D. Lewis, C. Mattos, A comprehensive survey of Ras mutations in cancer. *Cancer Res.* **72**, 2457–2467 (2012).
9. J. H. Jackson, J. W. Li, J. E. Buss, C. J. Der, C. G. Cochrane, Polylysine domain of K-ras 4B protein is crucial for malignant transformation. *Proc. Natl. Acad. Sci. U.S.A.* **91**, 12730–12734 (1994).
10. J. F. Hancock, A. I. Magee, J. E. Childs, C. J. Marshall, All ras proteins are polyisoprenylated but only some are palmitoylated. *Cell* **57**, 1167–1177 (1989).
11. J. F. Hancock, H. Paterson, C. J. Marshall, A polybasic domain or palmitoylation is required in addition to the CAAX motif to localize p21ras to the plasma membrane. *Cell* **63**, 133–139 (1990).
12. J. R. Silvius, F. l'Heureux, Fluorimetric evaluation of the affinities of isoprenylated peptides for lipid bilayers. *Biochemistry* **33**, 3014–3022 (1994).
13. R. Leventis, J. R. Silvius, Lipid-binding characteristics of the polybasic carboxy-terminal sequence of K-ras4B. *Biochemistry* **37**, 7640–7648 (1998).
14. J. R. Silvius, P. Bhagatji, R. Leventis, D. Terrone, K-ras4B and prenylated proteins lacking "second signals" associate dynamically with cellular membranes. *Mol. Biol. Cell* **17**, 192–202 (2006).
15. A. T. Baines, D. Xu, C. J. Der, Inhibition of Ras for cancer treatment: The search continues. *Future Med. Chem.* **3**, 1787–1808 (2011).
16. N. Berndt, S. M. Sebti, Measurement of protein farnesylation and geranylgeranylation in vitro, in cultured cells and in biopsies, and the effects of prenyl transferase inhibitors. *Nat. Protoc.* **6**, 1775–1791 (2011).
17. A. D. Cox, C. J. Der, M. R. Philips, Targeting RAS membrane association: Back to the future for anti-RAS drug discovery? *Clin. Cancer Res.* **21**, 1819–1827 (2015).
18. A. Chandra, H. E. Grecco, V. Pisupati, D. Perera, L. Cassidy, F. Skoulidis, S. A. Ismail, C. Hedberg, M. Hanzal-Bayer, A. R. Venkitaraman, A. Wittinghofer, P. I. H. Bastiaens, The GDI-like solubilizing factor PDE8 sustains the spatial organization and signalling of Ras family proteins. *Nat. Cell Biol.* **14**, 148–158 (2011).
19. M. Schmick, N. Vartak, B. Papke, M. Kovacevic, D. C. Truxius, L. Rossmannek, P. I. H. Bastiaens, KRAS localizes to the plasma membrane by spatial cycles of solubilization, trapping and vesicular transport. *Cell* **157**, 459–471 (2014).
20. P. Villalonga, C. López-Alcalá, M. Bosch, A. Chiloeches, N. Rocamora, J. Gil, R. Marais, C. J. Marshall, O. Bachs, N. Agell, Calmodulin binds to K-Ras, but not to H- or N-Ras, and modulates its downstream signaling. *Mol. Cell Biol.* **21**, 7345–7354 (2001).
21. M. Fivaz, T. Meyer, Reversible intracellular translocation of KRas but not HRas in hippocampal neurons regulated by Ca²⁺/calmodulin. *J. Cell Biol.* **170**, 429–441 (2005).
22. M.-T. Wang, M. Holderfield, J. Galeas, R. Delrosario, M. D. To, A. Balmain, F. M. Cormick, K-Ras promotes tumorigenicity through suppression of non-canonical Wnt signaling. *Cell* **163**, 1237–1251 (2015).
23. B. Sperlich, S. Kapoor, H. Waldmann, R. Winter, K. Weise, Regulation of K-Ras4B membrane binding by calmodulin. *Biophys. J.* **111**, 113–122 (2016).
24. N. Saito, N. Mine, D. W. Kufe, D. D. Von Hoff, T. Kawabe, CBP501 inhibits EGF-dependent cell migration, invasion and epithelial-to-mesenchymal transition of non-small cell lung cancer cells by blocking KRas to calmodulin binding. *Oncotarget* **8**, 74006–74018 (2017).
25. T. G. Bivona, S. E. Quatela, B. O. Bodemann, I. M. Ahearn, M. J. Soskis, A. Mor, J. Miura, H. H. Wiener, L. Wright, S. G. Saba, D. Yim, A. Fein, I. Pérez de Castro, C. Li, C. B. Thompson, A. D. Cox, M. R. Philips, PKC regulates a farnesyl-electrostatic switch on K-Ras that promotes its association with Bcl-XL on mitochondria and induces apoptosis. *Mol. Cell* **21**, 481–493 (2006).
26. S. E. Quatela, P. J. Sung, I. M. Ahearn, T. G. Bivona, M. R. Philips, Analysis of K-Ras phosphorylation, translocation, and induction of apoptosis. *Methods Enzymol.* **439**, 87–102 (2008).
27. P. J. Sung, F. D. Tsai, H. Vais, H. Court, J. Yang, N. Fehrenbacher, J. K. Foskett, M. R. Philips, Phosphorylated K-Ras limits cell survival by blocking Bcl-xL sensitization of inositol trisphosphate receptors. *Proc. Natl. Acad. Sci. U.S.A.* **110**, 20593–20598 (2013).
28. K.-j. Cho, D. E. Casteel, P. Prakash, L. Tan, D. van der Hoeven, A. A. Salim, C. Kim, R. J. Capon, E. Lacey, S. R. Cunha, A. A. Gorge, J. F. Hancock, AMPK and endothelial nitric oxide synthase signaling regulates K-Ras plasma membrane interactions via cyclic GMP-dependent protein kinase 2. *Mol. Cell Biol.* **36**, 3086–3099 (2016).
29. Y. Zhou, P. Prakash, H. Liang, K.-J. Cho, A. A. Gorge, J. F. Hancock, Lipid-sorting specificity encoded in K-Ras membrane anchor regulates signal output. *Cell* **168**, 239–251.e16 (2017).
30. G. Zimmermann, B. Papke, S. Ismail, N. Vartak, A. Chandra, M. Hoffmann, S. A. Hahn, G. Triola, A. Wittinghofer, P. I. H. Bastiaens, H. Waldmann, Small molecule inhibition of the KRAS-PDE8 interaction impairs oncogenic KRAS signalling. *Nature* **497**, 638–642 (2013).
31. P. Martin-Gago, E. K. Fansa, C. H. Klein, S. Murarka, P. Janning, M. Schürmann, M. Metz, S. Ismail, C. Schultz-Fademrecht, M. Baumann, P. I. H. Bastiaens, A. Wittinghofer, H. Waldmann, A PDE8-KRAS inhibitor chemotype with up to seven H-bonds and picomolar affinity that prevents efficient inhibitor release by Arl2. *Angew. Chem. Int. Ed. Engl.* **56**, 2423–2428 (2017).
32. H. Tidow, P. Nissen, Structural diversity of calmodulin binding to its target sites. *FEBS J.* **280**, 5551–5565 (2013).
33. C. B. Marshall, T. Nishikawa, M. Osawa, P. B. Stathopulos, M. Ikura, Calmodulin and STIM proteins: Two major calcium sensors in the cytoplasm and endoplasmic reticulum. *Biochem. Biophys. Res. Commun.* **460**, 5–21 (2015).
34. D. O'Connell, M. Bauer, C. B. Marshall, M. Ikura, S. Linse, Calmodulin, in *Encyclopedia of Metalloproteins*, R. H. Kretsinger, V. N. Uversky, E. A. Permyakov, Eds. (Springer, 2013).
35. M. Zhang, T. Tanaka, M. Ikura, Calcium-induced conformational transition revealed by the solution structure of apo calmodulin. *Nat. Struct. Biol.* **2**, 758–767 (1995).
36. C. Lopez-Alcala, B. Alvarez-Moya, P. Villalonga, M. Calvo, O. Bachs, N. Agell, Identification of essential interacting elements in K-Ras/calmodulin binding and its role in K-Ras localization. *J. Biol. Chem.* **283**, 10621–10631 (2008).
37. L.-J. Wu, L.-R. Xu, J.-M. Liao, J. Chen, Y. Liang, Both the C-terminal polylysine region and the farnesylation of K-RasB are important for its specific interaction with calmodulin. *PLOS ONE* **6**, e21929 (2011).
38. A. Banerjee, H. Jang, R. Nussinov, V. Gaponenko, The disordered hypervariable region and the folded catalytic domain of oncogenic K-Ras4B partner in phospholipid binding. *Curr. Opin. Struct. Biol.* **36**, 10–17 (2016).
39. H. Jang, A. Banerjee, T. Chavan, V. Gaponenko, R. Nussinov, Flexible-body motions of calmodulin and the farnesylated hypervariable region yield a high-affinity interaction enabling K-Ras4B membrane extraction. *J. Biol. Chem.* **292**, 12544–12559 (2017).
40. C. Agamasu, R. Ghirlando, T. Taylor, S. Messing, T. H. Tran, L. Bindu, M. Tonelli, D. V. Nissley, F. M. Cormick, A. G. Stephen, KRAS prenylation is required for bivalent binding with calmodulin in a nucleotide-independent manner. *Biophys. J.* **116**, 1049–1063 (2019).
41. M. Ikura, L. E. Kay, M. Krinks, A. Bax, Triple-resonance multidimensional NMR study of calmodulin complexed with the binding domain of skeletal muscle myosin light-chain kinase: Indication of a conformational change in the central helix. *Biochemistry* **30**, 5498–5504 (1991).
42. S. R. Martin, R. R. Biekofsky, M. A. Skinner, R. Guerrini, S. Salvadori, J. Feeney, P. M. Bayley, Interaction of calmodulin with the phosphofruktokinase target sequence. *FEBS Lett.* **577**, 284–288 (2004).
43. Z. Liu, H. J. Vogel, Structural basis for the regulation of L-type voltage-gated calcium channels: Interactions between the N-terminal cytoplasmic domain and Ca²⁺-calmodulin. *Front. Mol. Neurosci.* **5**, 38 (2012).
44. W. K. Gillette, D. Esposito, M. A. Blanco, P. Alexander, L. Bindu, C. Bittner, O. Chertov, P. H. Frank, C. Grose, J. E. Jones, Z. Meng, S. Perkins, Q. Van, R. Ghirlando, M. Fivash, D. V. Nissley, F. M. Cormick, M. Holderfield, A. G. Stephen, Farnesylated and methylated KRAS4b: High yield production of protein suitable for biophysical studies of prenylated protein-lipid interactions. *Sci. Rep.* **5**, 15916 (2015).
45. N. Hayashi, M. Matsubara, Y. Jinbo, K. Titani, Y. Izumi, N. Matsushima, Nef of HIV-1 interacts directly with calcium-bound calmodulin. *Protein Sci.* **11**, 529–537 (2002).
46. N. Hayashi, C. Nakagawa, Y. Ito, A. Takasaki, Y. Jinbo, Y. Yamakawa, K. Titani, K. Hashimoto, Y. Izumi, N. Matsushima, Myristoylation-regulated direct interaction between calcium-bound calmodulin and N-terminal region of pp60^{v-src}. *J. Mol. Biol.* **338**, 169–180 (2004).
47. K. P. Hoefflich, M. Ikura, Calmodulin in action: Diversity in target recognition and activation mechanisms. *Cell* **108**, 739–742 (2002).
48. M. Ikura, J. B. Ames, Genetic polymorphism and protein conformational plasticity in the calmodulin superfamily: Two ways to promote multifunctionality. *Proc. Natl. Acad. Sci. U.S.A.* **103**, 1159–1164 (2006).
49. M. Matsubara, T. Nakatsu, H. Kato, H. Taniguchi, Crystal structure of a myristoylated CAP-23/NAP-22 N-terminal domain complexed with Ca²⁺/calmodulin. *EMBO J.* **23**, 712–718 (2004).
50. K. L. Yap, J. Kim, K. M. Sherman, T. Yuan, M. Ikura, Calmodulin target database. *J. Struct. Funct. Genomics* **1**, 8–14 (2000).
51. M. J. Fischer, Amine coupling through EDC/NHS: A practical approach. *Methods Mol. Biol.* **627**, 55–73 (2010).
52. G. M. Clore, Practical aspects of paramagnetic relaxation enhancement in biological macromolecules. *Methods Enzymol.* **564**, 485–497 (2015).
53. S. Stoilova-McPhie, K. Grushin, D. Dalm, J. Miller, Lipid nanotechnologies for structural studies of membrane-associated proteins. *Proteins* **82**, 2902–2909 (2014).
54. M. T. Mazhab-Jafari, C. B. Marshall, M. J. Smith, G. M. C. Gasmis-Seabrook, P. B. Stathopulos, F. Inagaki, L. E. Kay, B. G. Neel, M. Ikura, Oncogenic and RASopathy-associated K-RAS

- mutations relieve membrane-dependent occlusion of the effector-binding site. *Proc. Natl. Acad. Sci. U.S.A.* **112**, 6625–6630 (2015).
55. Z. Fang, C. B. Marshall, T. Nishikawa, A. D. Gossert, J. M. Jansen, W. Jahnke, M. Ikura, Inhibition of K-RAS4B by a unique mechanism of action: Stabilizing membrane-dependent occlusion of the effector-binding site. *Cell Chem. Biol.* **25**, 1327–1336.e4 (2018).
 56. N. L. K. Pershing, B. L. Lampson, J. A. Belsky, E. Kaltenbrun, D. M. MacAlpine, C. M. Counter, Rare codons capacitate Kras-driven de novo tumorigenesis. *J. Clin. Invest.* **125**, 222–233 (2015).
 57. B. L. Lampson, N. L. K. Pershing, J. A. Prinz, J. R. Lacsina, W. F. Marzluff, C. V. Nicchitta, D. M. MacAlpine, C. M. Counter, Rare codons regulate KRas oncogenesis. *Curr. Biol.* **23**, 70–75 (2013).
 58. M. W. Berchtold, A. Villalobo, The many faces of calmodulin in cell proliferation, programmed cell death, autophagy, and cancer. *Biochim. Biophys. Acta* **1843**, 398–435 (2014).
 59. T. Zhu, K. Beckingham, M. Ikebe, High affinity Ca²⁺ binding sites of calmodulin are critical for the regulation of myosin β motor function. *J. Biol. Chem.* **273**, 20481–20486 (1998).
 60. P. Mukherjee, J. F. Maune, K. Beckingham, Interlobe communication in multiple calcium-binding site mutants of *Drosophila* calmodulin. *Protein Sci.* **5**, 468–477 (1996).
 61. H. Jang, A. Banerjee, K. Marcus, L. Makowski, C. Mattos, V. Gaponenko, R. Nussinov, The structural basis of the farnesylated and methylated KRas4B interaction with calmodulin. *Structure* **27**, 1647–1659.e4 (2019).
 62. L. Emmanouilidis, U. Schütz, K. Tripsianes, T. Madl, J. Radke, R. Rucktäschel, M. Wilmanns, W. Schliebs, R. Erdmann, M. Sattler, Allosteric modulation of peroxisomal membrane protein recognition by farnesylation of the peroxisomal import receptor PEX19. *Nat. Commun.* **8**, 14635 (2017).
 63. K. T. Lane, L. S. Beese, Thematic review series: Lipid posttranslational modifications. Structural biology of protein farnesyltransferase and geranylgeranyltransferase type I. *J. Lipid Res.* **47**, 681–699 (2006).
 64. S. Dharmiah, L. Bindu, T. H. Tran, W. K. Gillette, P. H. Frank, R. Ghirlando, D. V. Nissley, D. Esposito, F. M. Cormick, A. G. Stephen, D. K. Simanshu, Structural basis of recognition of farnesylated and methylated KRAS4b by PDE δ . *Proc. Natl. Acad. Sci. U.S.A.* **113**, E6766–E6775 (2016).
 65. E. Yamauchi, T. Nakatsu, M. Matsubara, H. Kato, H. Taniguchi, Crystal structure of a MARCKS peptide containing the calmodulin-binding domain in complex with Ca²⁺-calmodulin. *Nat. Struct. Biol.* **10**, 226–231 (2003).
 66. S. M. Elsaraj, R. P. Bhullar, Regulation of platelet Rac1 and Cdc42 activation through interaction with calmodulin. *Biochim. Biophys. Acta* **1783**, 770–778 (2008).
 67. M. Vidal-Quadras, M. Gelabert-Baldrich, D. Soriano-Castell, A. Lladó, C. Rentero, M. Calvo, A. Pol, C. Enrich, F. Tebar, Rac1 and calmodulin interactions modulate dynamics of ARF6-dependent endocytosis. *Traffic* **12**, 1879–1896 (2011).
 68. B. Xu, P. Chelikani, R. P. Bhullar, Characterization and functional analysis of the calmodulin-binding domain of Rac1 GTPase. *PLOS ONE* **7**, e42975 (2012).
 69. O. Rocks, A. Peyker, M. Kahms, P. J. Vermeer, C. Koerner, M. Lumbierres, J. Kuhlmann, H. Waldmann, A. Wittinghofer, P. I. H. Bastiaens, An acylation cycle regulates localization and activity of palmitoylated Ras isoforms. *Science* **307**, 1746–1752 (2005).
 70. O. Rocks, A. Peyker, P. I. H. Bastiaens, Spatio-temporal segregation of Ras signals: One ship, three anchors, many harbors. *Curr. Opin. Cell Biol.* **18**, 351–357 (2006).
 71. O. Rocks, M. Gerauer, N. Vartak, S. Koch, Z.-P. Huang, M. Pechlivanis, J. Kuhlmann, L. Brunsfeld, A. Chandra, B. Ellinger, H. Waldmann, P. I. H. Bastiaens, The palmitoylation machinery is a spatially organizing system for peripheral membrane proteins. *Cell* **141**, 458–471 (2010).
 72. B. M. M. Grant, C. B. Marshall, M. Ikura, Expression and purification of calmodulin for NMR and other biophysical applications. *Methods Mol. Biol.* **1929**, 207–221 (2019).
 73. Y. Kano, T. Gebregiworgis, C. B. Marshall, N. Radulovich, B. P. K. Poon, J. St-Germain, J. D. Cook, I. Valencia-Sama, B. M. M. Grant, S. G. Herrera, J. Miao, B. Raught, M. S. Irwin, J. E. Lee, J. J. Yeh, Z.-Y. Zhang, M.-S. Tsao, M. Ikura, M. Ohh, Tyrosyl phosphorylation of KRAS stalls GTPase cycle via alteration of switch I and II conformation. *Nat. Commun.* **10**, 224 (2019).
 74. A. D. Gossert, W. Jahnke, Isotope labeling in insect cells. *Adv. Exp. Med. Biol.* **992**, 179–196 (2012).
 75. A. D. Gossert, A. Hinniger, S. Gutmann, W. Jahnke, A. Strauss, C. Fernández, A simple protocol for amino acid type selective isotope labeling in insect cells with improved yields and high reproducibility. *J. Biomol. NMR* **51**, 449–456 (2011).
 76. Z. Otwinowski, W. Minor, Processing of X-ray diffraction data collected in oscillation mode. *Methods Enzymol.* **276**, 307–326 (1997).
 77. P. Emsley, B. Lohkamp, W. G. Scott, K. Cowtan, Features and development of Coot. *Acta Crystallogr. D Biol. Crystallogr.* **66**, 486–501 (2010).
 78. P. D. Adams, P. V. Afonine, G. Bunkóczi, V. B. Chen, I. W. Davis, N. Echols, J. J. Headd, L.-W. Hung, G. J. Kapral, R. W. Grosse-Kunstleve, A. J. McCoy, N. W. Moriarty, R. Oeffner, R. J. Read, D. C. Richardson, J. S. Richardson, T. C. Terwilliger, P. H. Zwart, PHENIX: A comprehensive python-based system for macromolecular structure solution. *Acta Crystallogr. D Biol. Crystallogr.* **66**, 213–221 (2010).
 79. Y. Kobashigawa, K. Harada, N. Yoshida, K. Ogura, F. Inagaki, Phosphoinositide-incorporated lipid-protein nanodiscs: A tool for studying protein-lipid interactions. *Anal. Biochem.* **410**, 77–83 (2011).
 80. J. Goedhart, L. van Weeren, M. A. Hink, N. O. E. Vischer, K. Jalink, T. W. J. Gadella Jr., Bright cyan fluorescent protein variants identified by fluorescence lifetime screening. *Nat. Methods* **7**, 137–139 (2010).
 81. G.-J. Kremers, J. Goedhart, E. B. van Munster, T. W. J. Gadella Jr., Cyan and yellow super fluorescent proteins with improved brightness, protein folding, and FRET Förster radius. *Biochemistry* **45**, 6570–6580 (2006).
 82. F. Guo, M.-Y. Chiang, Y. Wang, Y.-Z. Zhang, An in vitro recombination method to convert restriction- and ligation-independent expression vectors. *Biotechnol. J.* **3**, 370–377 (2008).
 83. J. Schindelin, I. Arganda-Carreras, E. Frise, V. Kaynig, M. Longair, T. Pietzsch, S. Preibisch, C. Rueden, S. Saalfeld, B. Schmid, J.-Y. Tinevez, D. J. White, V. Hartenstein, K. Eliceiri, P. Tomancak, A. Cardona, Fiji: An open-source platform for biological-image analysis. *Nat. Methods* **9**, 676–682 (2012).

Acknowledgments: We thank the staff at the Advanced Optical Microscopy Facility, University Health Network for the help with this project. Research described in this paper was performed using beamline 08ID-1 at the Canadian Light Source, which is supported by the Canada Foundation for Innovation (CFI), Natural Sciences and Engineering Research Council of Canada, the University of Saskatchewan, the Government of Saskatchewan, Western Economic Diversification Canada, the National Research Council Canada, and the Canadian Institutes of Health Research. We thank D. Gadella and Y.-Z. Zhang for the donations of plasmids and D. Esposito at the NCI for providing the baculovirus expression system for production of fully processed KRAS. We thank G. Gasmi-Seabrook for assistance and management of the Princess Margaret NMR facility funded by the CFI and the Princess Margaret Cancer Foundation (PMCF). We also thank K. Hueniken, Research Analyst at the University Health Network in the Department of Biostatistics, for consultation on statistical analysis. **Funding:** This work was supported by grants from the Canadian Institutes of Health Research (410008598), the Canadian Cancer Society Research Institute (703209 and 706696), and the Heart and Stroke Foundation of Canada (G-16-00014035). In addition, we thank the CFI, PMCF, and Canada Research Chairs for funding and support. **Author contributions:** B.M.M.G., C.B.M., M.E., and M.I. conceived the presented ideas. B.M.M.G., C.B.M., and M.E. developed and planned the experiments. B.G., M.E., S.-I.B., and T.G. conducted the experiments, processed and analyzed the data, and produced the figures. K.-Y.L., T.G., and N.I. assisted with conceptualization and advanced protocols. C.B.M. and M.I. supervised the project. B.G. drafted the initial manuscript and edited it with the help of C.B.M., M.E., and M.I. All authors provided useful critiques and feedback on the project and manuscript. **Competing interests:** The authors declare that they have no competing interests. **Data and materials availability:** The structure of calcium-bound CaM in complex with FCME has been deposited in PDB (PDB ID: 6O54). **Data and materials availability:** All other data needed to evaluate the conclusions in the paper are present in the paper or the Supplementary Materials.

Submitted 14 August 2019

Accepted 10 March 2020

Published 31 March 2020

10.1126/scisignal.aaz0344

Citation: B. M. M. Grant, M. Enomoto, S.-I. Back, K.-Y. Lee, T. Gebregiworgis, N. Ishiyama, M. Ikura, C. B. Marshall, Calmodulin disrupts plasma membrane localization of farnesylated KRAS4b by sequestering its lipid moiety. *Sci. Signal.* **13**, eaaz0344 (2020).

Calmodulin disrupts plasma membrane localization of farnesylated KRAS4b by sequestering its lipid moiety

Benjamin M. M. Grant, Masahiro Enomoto, Sung-In Back, Ki-Young Lee, Teklab Gebregiworgis, Noboru Ishiyama, Mitsuhiro Ikura and Christopher B. Marshall

Sci. Signal. **13** (625), eaaz0344.
DOI: 10.1126/scisignal.aaz0344

How Ca²⁺ inhibits KRAS

The RAS protein family regulates cell proliferation, differentiation, and survival. Mutations in RAS proteins are frequently implicated in driving tumor growth. Grant *et al.* resolved the structure of the C terminus of the RAS isoform KRAS4b in complex with the Ca²⁺-sensing protein calmodulin (CaM) and developed FRET sensors to explore the interaction in cells. They found that a farnesylated region of KRAS4b was bound in a hydrophobic pocket of CaM in response to increased intracellular Ca²⁺, thereby sequestering KRAS4b away from the membrane and dampening its output. Exploiting this sequestration mechanism might yield a new way to inhibit KRAS signaling.

ARTICLE TOOLS

<http://stke.sciencemag.org/content/13/625/eaaz0344>

SUPPLEMENTARY MATERIALS

<http://stke.sciencemag.org/content/suppl/2020/03/27/13.625.eaaz0344.DC1>

RELATED CONTENT

<http://stke.sciencemag.org/content/sigtrans/11/546/eaar8371.full>

REFERENCES

This article cites 82 articles, 18 of which you can access for free
<http://stke.sciencemag.org/content/13/625/eaaz0344#BIBL>

PERMISSIONS

<http://www.sciencemag.org/help/reprints-and-permissions>

Use of this article is subject to the [Terms of Service](#)

Science Signaling (ISSN 1937-9145) is published by the American Association for the Advancement of Science, 1200 New York Avenue NW, Washington, DC 20005. The title *Science Signaling* is a registered trademark of AAAS.

Copyright © 2020 The Authors, some rights reserved; exclusive licensee American Association for the Advancement of Science. No claim to original U.S. Government Works